Title
Spectral Temporal LiDAR and Optical Dynamic Range Compression; New Concepts in Photonics

Author
Jiang, Yunshan

Publication Date
2018

Peer reviewed|Thesis/dissertation

UNIVERSITY OF CALIFORNIA

Los Angeles

Spectral Temporal LiDAR and Optical Dynamic Range Compression; New Concepts in Photonics

A dissertation submitted in partial satisfaction
of the requirements for the degree
Doctor of Philosophy in Electrical and Computer Engineering

by

Yunshan Jiang

2018

ABSTRACT OF THE DISSERTATION

Spectral Temporal LiDAR
and Optical Dynamic Range Compression;
New Concepts in Photonics

by

Yunshan Jiang
Doctor of Philosophy in Electrical and Computer Engineering
University of California, Los Angeles, 2018
Professor Bahram Jalali, Chair

Photonic time-stretch, invented at UCLA, has established world's fastest real-time spectrometers and cameras with applications in biological cell screening, tomography, microfluidics, velocimetry and vibrometry. Time stretch instruments have led to several scientific breakthroughs including the discoveries of optical rogue waves, relativistic electron bunching in synchrotrons, and first ever observations of the birth of laser mode-locking and internal motion of soliton molecules. In time-stretch imaging, the target's spatial information is encoded in the spectrum of the ultrafast laser pulses, which is stretched in time and then detected by a single-pixel detector and digitized by a real-time ADC, and processed by a CPU or a dedicated FPGA or GPU. Various methods have been proposed to realize time stretch, including single mode fibers, dispersion compensating fibers, chirped Bragg grating, and chromo-modal dispersion. However, none of those methods provide chirp with a large time-bandwidth product, which limits the time/depth range the pulse can measure.

In this study, we demonstrate a discrete time-stretch method that can generate the giant time-bandwidth product with arbitrary nonlinear chirp for operating wavelength from the visible to the infrared. We show its application in warped-stretch (foveated) imaging and a time-of-flight LIDAR with ∼MHz refresh rate.

Most optical sensing and measurement techniques suffer from the limited dynamic range. In a second and related project, we have proposed the concept of optical dynamic range com-

pression. This powerful technique provides a mean to match the dynamic range of the signal to that of the detector and data converter, leading to improved signal to noise ratio and a wider dynamic range. We outline various methods to implement optical dynamic range compression using nonlinear optics, silicon photonics and saturated amplifications.

The dissertation of Yunshan Jiang is approved.

Mona Jarrahi

Chang Jin Kim

Oscar M. Stafsudd

Bahram Jalali, Committee Chair

University of California, Los Angeles

2018

To Lianxin, Guilian, Jun, and Tori

TABLE OF CONTENTS

LIST OF FIGURES

LIST OF TABLES

ACKNOWLEDGMENTS

First and foremost, I would like to express my sincere gratitude to my advisor, Prof. Bahram Jalali, for his immeasurable amount of support and guidance. His passion for science, dedication for research and education, and deep knowledge of numerous fields have always inspired me. His training has significantly influenced my character both in professional and personal life. Also, I would like to thank my other committee members, Prof. Stafsudd, Prof. Jarrahi, and Prof. Kim, for their invaluable time and feedback.

I would like to thank impressive students and postdoctoral researchers of Prof. Jalali's research laboratory, who I have learned a lot from. Specifically, Peter DeVore, Ata Mahjoubfar and Nino Karpf had a significant influence on shaping me into a scientist. Also, I am very thankful to my colleagues in the group, including Brandon Buckley, Daniel Lam, Claire Lifan Chen, Cejo Lonappan, Jacky Chan, and Madhuri Suthar for the helpful discussions that we had. I would like to express my appreciation for the help from the lab members, especially Saili Zhao, Sifeng He, Shuqian Sun, and Tingyi Zhou, who have dedicated significant amount of time and effort to my project.

I would like to thank all of my publication co-authors, which our works consist many chapters of this dissertation. Chapter 2 is a version of Optics Letters, Vol. 41, Issue 6, 1273-1276, 2016. Chapter 3 is a version of Applied Physics Letter Photonics, Vol. 3, Issue 11, 110806, 2018. Chapter 4 is a version of the manuscript we are preparing for submitting to a journal. Most of the projects are funded by the Office of Naval Research (ONR) MURI Program on Near-Field Nanophotonics for Energy Efficient Computing and Communication (NECom).

VITA

2009–2013 B.S. Optical Engineering (Chu Kochen Honors College), Zhejiang, China

2013–2015 M.S., Electrical Engineering, University of California, Los Angeles, US

2015–2017 Teaching assistant, University of California, Los Angeles, US

2015–present Graduate Student Researcher, Electrical Engineering, University of California, Los Angeles, US

PUBLICATIONS

Y. Jiang, S. Karpf, Jalali, *Time-stretch foveated LIDAR*, in preparation

Y. Jiang, S. Zhao, B. Jalali, *Invited Article: Optical Dynamic Range Compression*, APL Photonics, 2018

Y. Jiang, P. Devore, B. Jalali, *Analog Optical Computing Primitives in Silicon Photonics*, Optics Letters, 2016

B. Jalali, S. Karpf, B. Rice, Y. Jiang, *Spectro-temporal LIDAR, U.S. Provisional Patent Application*, No.62/641. 964, 2018

B. Jalali, Y. Jiang, *A method for coherent optical ranging and velocimetry*, in preparetion

Jiang, Yunshan, and Bahram Jalali. *Optical dynamic range compression (Conference Presentation).* In Real-time Measurements, Rogue Phenomena, and Single-Shot Applications III, vol. 10517, p. 105170I. International Society for Optics and Photonics, 2018.

Y. Jiang and B. Jalali, *Optical Companding*, in Conference on Lasers and Electro-Optics, OSA Technical Digest (online), paper SM4D.5, Optical Society of America, 2018.

Y. Jiang and B. Jalali, *Compressing the dynamic range and statistics of optical signals* in CLEO Pacific Rim Conference 2018, OSA Technical Digest, paper Tu2D.1, Optical Society

of America, 2018.

Y. Jiang, P. T. DeVore, C. K. Lonappan, J. Adam, and B. Jalali. *SiCloud: An online education tool for silicon photonics.* In Education and Training in Optics and Photonics, p. 104521Q. Optical Society of America, 2017.

Y. Jiang, P. T. S. DeVore, A. Mahjoubfar and B. Jalali, *Signal De-convolution with analog logarithmic computing primitives in silicon photonics* 2016 IEEE Photonics Society Summer Topical Meeting Series (SUM), Newport Beach, CA, 2016

Y. Jiang, P. T. Devore, A. Mahjoubfar, and B. Jalali. *Analog logarithmic computing primitives with silicon photonics* In CLEO: Applications and Technology, pp. JW2A-114. Optical Society of America, 2016.

CHAPTER 1

Introduction

Optical systems with fast speed, high sensitivity, and a large dynamic range are desired in nearly all optical sensing and communication applications. For example, in Light Detection and Ranging (LiDAR) systems, the accurate mapping of the fast-evolving environment with a large detection range necessitates detectors with a large bandwidth and a large dynamic range. However, as limited by the fundamental trade-off between the speed and the dynamic range (measured in the effective number of bits) of real-time analog-to-digital converters (ADC) [1, 2], high speed comes at the price of low sensitivity and less accuracy (as shown in Figure 1.1).

Photonic time-stretch, invented at UCLA, is the most successful non-electronic method to alleviate the ADC speed limitations by slowing down the signal prior to digitization [3–5]. In time-stretch imaging [6], the target's spatial information is encoded in the spectrum of the ultrafast laser pulses, which is stretched continuously in time by propagating through dispersion and then detected by a single-pixel detector. Lateral positions of pixels are identified through a one-to-one correspondence between the time samples and their corresponding optical frequencies which are mapped into time. Distrubuted Raman amplification [7] can be induced in the dispersive fiber to compensate for the large loss during propagation.

Although the conventional time-stretch is a proven and successful microscopy technique, it is not well suited for LiDAR imaging. In ranging applications based on time of flight, the arrival time of photons is determined by the axial position of the target and there is no unique mapping between time, wavelength and lateral position. To remove the resulting ambiguity, independent knowledge of both time and wavelength is required in order to acquire three-dimensional information of the target. This requires the use of a high speed spec-

trometer as a receiver which is highly impractical. Applications of time stretch imaging to LiDAR is further hindered because the laser power is spread across the field of view resulting in low optical power per pixel. Optical amplifiers like Raman amplificaiton can help with the measurement of the weak signals by boosting lower portion of the dynamic range above noise floor, but it also amplifies the strong signals and requires the receiver to have a larger dynamic range. In LiDAR systems, the power of the returned signal decays quadratically with the distance, so a dynamic range compression technique which is able to enhance the small amplitudes without boosting the large amplitudes is desired to extend the maximum detection range.

In chapter 2, we propose and demonstrate a new type of LiDAR that employs the discrete

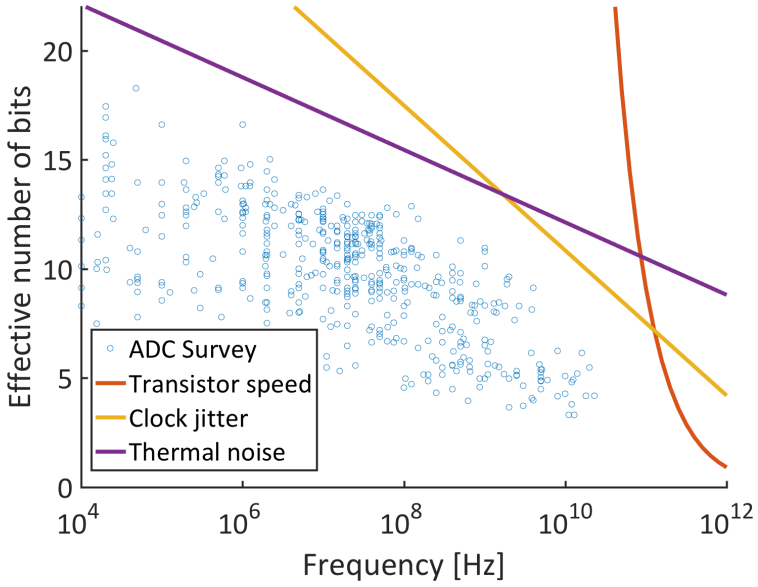

Figure 1.1: The tradeoff between frequency and dynamic range in ADCs. As the sampling rate of an ADC increases, its dynamic range, measured by the effective number of bits, reduces. The performance of the ADCs designed for low frequencies is often limited by the aggregate thermal noise. As for high speed ADCs, the limitations are mainly caused by the clock jitter and the limited gain bandwidth of transistors. The ADC survey is from Ref. [1]

time-stretch technique which does not suffer from the aforementioned problems in the conventional time stretch methods. Using a spectro-temporally encoded illumination pattern , our LiDAR realizes non-mechanical scanning in one dimension with ∼MHz line rate with a

high number of pixels per line. Unlike conventional time stretch methods where the chirp comes from the dispersion in the propagation media, the discrete time stretch method is able to produce arbitrary chirp profiles with a giant time-bandwidth product, and allow imaging with visions that adapts dynamically to signal sparsity, reducing the massive amount of data generated at the high imaging speed. We showed two different implementations of the time-stretch LiDAR, the first with a supercontinuum pulsed source at 1550nm and the second with a frequency-domain-mode-locked laser at 1060nm.

In chapter 3, we proposed the concept of optical dynamic range compression. This powerful technique provides an optical solution to alleviate the burden on the dynamic range during data acquisition. By reshaping the signal's amplitudes through a logarithmic-like transformation, the technology provides a mean to match the dynamic range of the signal to that of the detector and data converter, leading to an improved signal to noise ratio and a wider dynamic range. We talked about its utilities in non-uniform quantization, reshaping signal's statistical distribution, and extending the detection range in LiDAR systems. We outline various methods to implement optical dynamic range compression using nonlinear optics, silicon photonics and saturated amplifications.

In chapter 4, we applied the concept of optical signal processing to computing. We show an approach to implementing logarithmic-type analog co-processors in silicon photonics and use it to perform the exponentiation operation and the recovery of a signal in the presence of multiplicative distortion. The function is realized by exploiting nonlinear-absorption-enhanced Raman amplification saturation in a silicon waveguide.

CHAPTER 2

Time-stretch foveated LiDAR with spectral-temporal encoding

2.1 Introduction

Emerging civilian applications such as autonomous driving, cleantech (wind turbines), industrial automation, and facial recognition have fueled great interest in high resolution 3D imaging. LiDAR, the optical implementation of RADAR is a remote sensing method for measuring distance and velocity and is one of leading candidates for these applications. By scanning the laser beam, LiDAR systems acquire a 3D map of their surrounding environment.

Traditional methods based on the mechanical scanning [8] and are inherently slow, bulky, and prone to failure and are not well suited for the emerging applications. LiDAR designs with no moving parts (inertia-free) are desirable for fast steering and immunity against vibrations [9]. Inspired by microwave phased array antennas, one such approach for beam steering is the use of an optical phase array [10–12]. Practical implementations of this technique is hindered by difficulties in accurate control of optical phase which is exceedingly more difficult at the much higher optical frequencies. In all LiDARs, the extremely weak returned signals necessitate detectors with internal gain and low noise, such as Avalanche Photodiodes (APDs) or Photomultipliers Tubes (PMTs). This favors single pixel imaging systems because realization of APDs and PMT arrays are difficult.

Spectral-encoded illumination, typically implemented using a broadband pulsed laser and diffractive optics, offers non-mechanical scanning [13]. However, a spectrometer is required at the receiver increasing the cost and complexity as well as limiting the speed. Photonic

time stretch is a high speed data acquisition method [3, 4] that has been highly successful in continuous single shot measurements of fast changing dynamical events [14–19] and ultrafast imaging [6, 20–24]. Lateral positions of pixels are identified through a one-to-one correspondence between the time samples and their corresponding optical frequencies which are mapped into time. Conventional time stretch imaging enjoys the benefits of spectral encoding but works with a single-pixel detector which is fast and simple to implement. However, its application to LiDAR is hindered because of the one-to-one mapping of time-to-wavelength-to-lateral position. In ranging applications based on time of flight, the arrival time of photons is determined by the axial position of the target and there is no unique mapping between time, wavelength and lateral position. To remove the resulting ambiguity, independent knowledge of both time and wavelength is required in order to acquire three-dimensional information of the target. This requires the use of a high speed spectrometer in the Lidar receiver which is highly impractical. Applications of time stretch imaging to LiDAR is further hindered because the laser power is spread across the field of view resulting in low optical power per pixel. Therefore, the conventional time stretch is a proven and successful microscopy technique but is not well suited for ranging applications.

Here we proposed a LiDAR that employs time-stretch technique but does not suffer from the aforementioned problems. It realizes inertia-free scanning in one dimension using a single laser and a single pixel detector and achieves imaging at $\sim$MHz line rate with a high number of pixels. It also achieves adaptive foveated vision (AFV) with an dynamically adjustable field of view (FoV) and resolution. A spectro-temporal-encoded laser source is dispersed into discrete collimated beams in space, illuminating different angular positions in sequence with high peak power. Spectral encoding eliminates mechanical scanning in one-dimension and the need for a spectrometer on the detection side is eliminated by employing temporal encoding. We demonstrated two different implementations of this LiDAR system, the first with a supercontinuum pulsed source at 1550nm and the second with a frequency-domain-mode-locked(FDML) laser with a master oscillator power amplifier(MOPA) at 1060nm.

2.2 Non-mechanical beam steering with a spectro-temporal encoded source

The concept of the Time-stretch Foveated LiDAR is illustrated in Figure 2.1. A spectro-temporal modulator configures the output of a broadband source into a discrete spectro-temporal pattern comprising a train of pulses of varying central frequencies and a fixed temporal interval. The source is diffracted into collimated beams to illuminate different angular positions with a high peak power. The three-dimensional information of the target is encoded onto the time domain of the returned spectro-temporal echoes, where the angular position and the reflectivity is mapped to wavelengths that located in different time windows (ΔT_i), and the depth distance is measured by the delay between the echo pulse and the illumination pulse (δt_i) within each time window. Spectro-temporal encoding eliminates the ambiguity of mapping between time, wavelength and lateral position in spectral LiDAR imaging and permit single-pixel detection in only the time domain. Our time-stretch foveated LiDAR also allows imaging with visions that adapts dynamically to the fast-evolving scene. We achieve foveal vision by creating sources with a non-uniformly sampled spectrum that generates a warped spatial illumination pattern. This exploits the sparsity of the image by efficiently assigning more pixels in the information-rich regions of the scene.

The depth and angular detection range of time-stretch LiDAR is determined by the discrete chirp-time-bandwidth product. The maximum depth (L_{max}) is limited by the temporal interval between spectro-temporally multiplexed pulses (ΔT):

$$Ł_{max} = \frac{c}{2} * \Delta T = \frac{c}{2 * f_{rep} * N} = \frac{c * T_{chirp}}{2 * N} \tag{2.1}$$

where c is the speed of light, f_{rep} is the repetition rate of the laser, N is number of wavelengths channels, and $T_{chirp} = \frac{1}{f_{rep}}$ is defined as the discrete chirp time. Assuming channel number of 100, the maximum detection range can be tuned freely from 1 meter to 300 meters by changing the laser's repetition rate from 1.5 MHz to 5 kHz. The maximum angular range or the field of view (FoV) is determined by the sweeping bandwidth of the source as well as the spatial dispersion (D). The detectable range of the proposed LiDAR, as described by the product of the pixel number (N), maximum depth range and FoV, is proportional to the

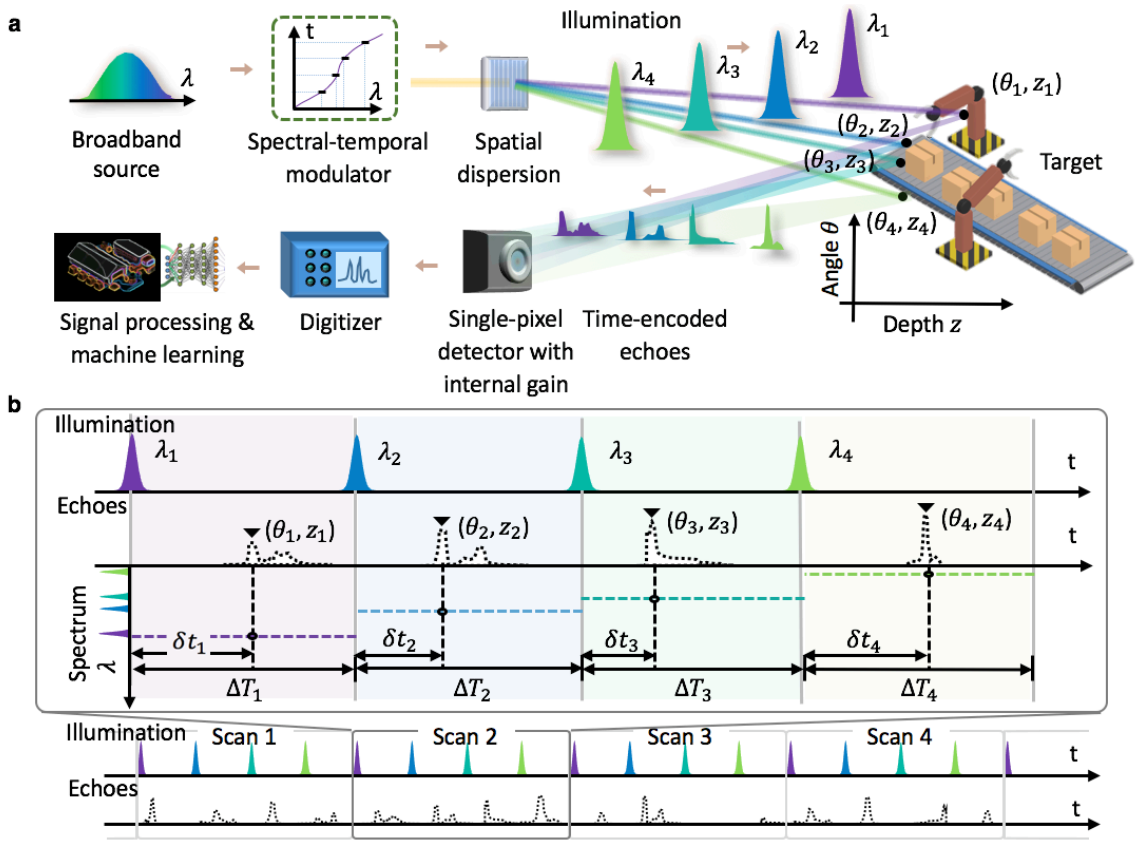

Figure 2.1: Time-stretch LiDAR enables inertia-free imaging in one dimension at MHz line rate with high resolution, adaptive foveated vision, and adjustable field-of-view (or scale invariant digital zoom) with a single laser and a single pixel detector. (a), A broadband source is spectro-temporal modulated into a train of discrete pulses with varying central wavelengths. The spectro-temporally multiplexed pulses are diffracted in space to discrete collimated beams so that different wavelengths (λ_i) illuminate pixels at different angular positions (θ_i) at the beginning of each corresponding time window (ΔT_i). The returned spectro-temporal echoes are received by a single-pixel detector with internal gain and digitally processed to recover the depth image. (b), Spectro-temporal encoding eliminates the ambiguity of mapping between time, wavelength and lateral position in spectral LiDAR imaging and permit single-pixel detection. Both the target's angular and depth information is encoded in the temporal domain of the spectro-temporal echoes. The angular positions and the reflectivity are mapped to wavelengths that are located in different temporal windows (ΔT_i). The depth information is recorded as the delay δt_i between the echo and illumination pulses inside each temporal window. By using a source with non-uniform spectrum, a foveated image can be generated where more pixels are assigned to the information-rich area.

discrete-chirp-time-bandwidth product (TBP).

$$N * L_{max} * FoV = \frac{c * D}{2} * (T_{chirp} * \Delta\lambda) \tag{2.2}$$

A source with a large TBP is necessary for outdoor applications where a large depth and angular range are needed. For example, a detection range of 10m with 6°field-of-view and 60 channels require a source with 1us chirp time and 1500GHz bandwidth (assuming dispersion of 0.5°/nm and operation wavelength at 1550nm), which corresponds to a TBP of $6 * 10^6$. Time-stretch LiDAR places rigorous requirements on the laser source to have tens of nanometer sweeping bandwidth and repetition rate of ∼MHz with a giant TBP of more than 10^6, which is not easily feasible with off-shelf optical sources. Conventional tunable CW lasers that rely on an electro-mechanically tuned external cavity provide a large sweeping bandwidth of over 100nm, but usually has a repetition rate below 1 kHz [25]. Mode-locked lasers typically produce ultrafast pulses with a broad bandwidth at repetition rate above 20MHz and this high repetition range limits the LiDAR range to ∼cm. While the repetition rate can be reduced by pulse picking, large enough chirp durations cannot be achieved using dispersive fibers which are an integral part of classical time stretch systems [3]. Various methods have been demonstrated to realize time-stretch, including single mode fibers, dispersion compensating fibers, chirped Bragg gratings [26], and chromo-modal dispersion (CMD) [27]. As the large dispersion comes at the price of high propagation loss, the achievable time bandwidth product is low by two orders of magnitude. In below, we demonstrate two implementations of the time-stretch LiDAR that achieve time bandwidth products of over 10^6.

2.3 Time-stretch foveated LiDAR based on true-time delay

The first implementation is based on the true-time delay method to achieve discrete time stretch. It utilized a gain-switch supercontinuum laser and an arrayed waveguide grating to create wavelength encoded discrete delays. Unlike previous implementations of time stretch

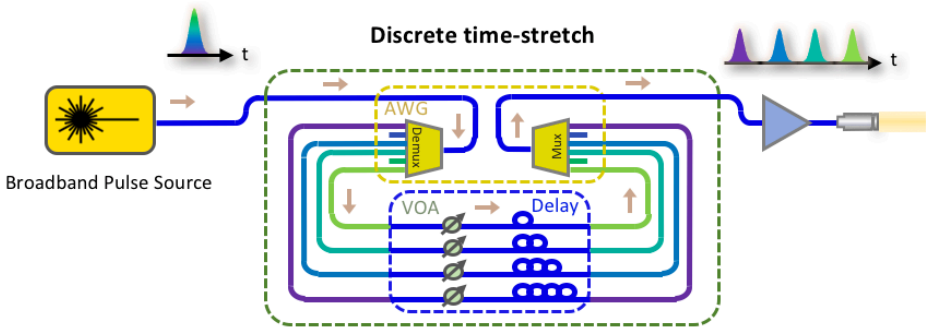

Figure 2.2: Implementation 1 with the true-time delay method. It generates spectro-temporal-encoded illumination for the time-stretch LiDAR with a giant time-bandwidth product and an adaptive warped chirp profile. The broadband pulses from a gain-switched supercontinuum laser is optically demultiplexed (DeMUX) by an arrayed waveguide grating (AWG) into a plurality of wavelengths, delayed by single mode fibers with varying lengths, equalized by the variable optical attenuators (VOA), and combined by a multiplexer (MUX) with symmetric transmission spectra. The generated pulse train is amplified by a fiber based optical amplifier to high peak power for the next sensing stage. As compared to the conventional time stretch methods utilizing material dispersion and don't allow long chirp time, discrete time-stretch method is based on wavelength-dependent true time delay and can achieve a giant discrete-chirp-time-bandwidth product over 10^6, which enables LiDAR imaging with a large depth and angular range. An arbitrary spectrum-to-time mapping is realized by nonuniformly sampling the spectrum and connecting discrete wavelengths to the corresponding true time delays. This adaptive warped chirp profile can provide a non-uniform illumination pattern in time-stretch LiDAR.

where the chirp comes from the propagation in a lossy dispersive media, the proposed method decouples chirp from the dispersion property of the medium, enabling arbitrary nonlinear chirp profiles and a giant TBP, and can be applied to a large range of operation wavelengths. The implementation is based on a recirculating photonic filter (RPF) [28], that samples the spectrum in a designated profile and assigns each wavelength a true time delay that is a function of frequency, as shown in Figure 2.2. Spectro-temporal patterns with a tunable warped chirp profile are realized by switching the discrete wavelengths between various delays. We demonstrate spectrum-to-time mapping in a linear, sublinear, superlinear, and non-monotonic function with a giant TBP over $3 * 10^6$ (as shown in Figure 2.3). The method provide a target-specific nonlinear discrete stretch for the Serial time-encoded amplified imaging system (STEAM) [6], as shown in Figure 2.4. Discrete time stretch that based on the true-time delay method enables a foveated (warped) imaging in STEAM system. As compared to the conventional time stretch where the chirp comes from material dispersion of the DCF fiber, the discrete time stretch enables a target-specific non-uniform illumination that reduces the massive amount of data generated in high-speed imaging. It can also compensate for the nonlinear diffraction caused by the grating to provide a linear space-to-wavelength-to time mapping, which is not possible in conventional time-stretch systems and requires post-processing digitally.

LiDAR based on true-time delay method permit inertia-free imaging with an adaptive foveated vision and optical compression, as shown in Figure 2.5. A gain-switched laser centered at 1550nm with 1 MHz repetition rate is modulated into spectra-temporal pattern with a 33 ns temporal interval and 12nm sweeping bandwidth, resulting in a TBP of $1.5 * 10^6$. This permits a maximum detection range of 5m. A FOV of 6°in the horizontal direction is realized by using a diffraction grating with 0.5°/nm spatial dispersion. The vertical direction is scanned mechanically. In Figure 2.5 (a-b), a train of 30 spectro-temporal pulses with a fixed 0.4nm frequency spacing generates image with a uniform sampling in the horizontal direction at a line rate of 1 MHz. While high-speed imaging is preferable to capture fast movements and improve image quality via averaging, it inevitably creates a massive amount of data and can overwhelm the processing backend [26,29,30]. Foveated illumination achieved

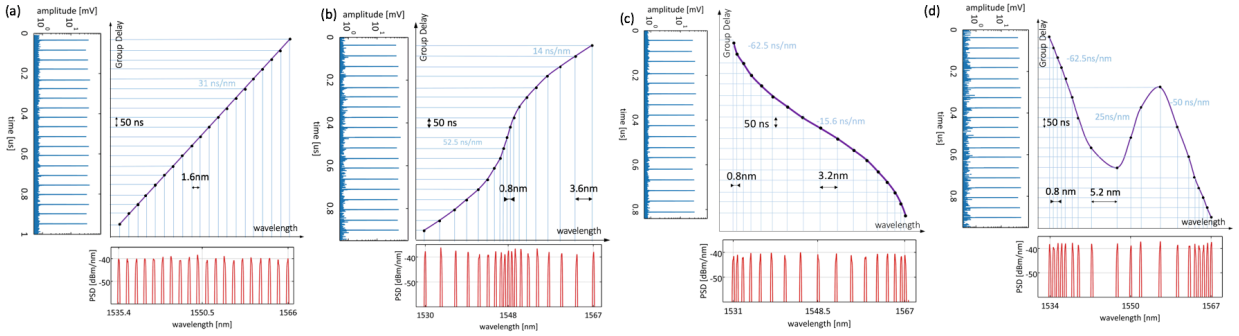

Figure 2.3: Discrete time-stretch method based on true-time delay configures the output of a gain-switched supercontinuum source centered at 1550nm to spectral-temporal patterns with arbitrary chirp profiles with a long chirp time of over 1us, a large sweep bandwidth of 30nm, resulting in a giant chirped-time-bandwidth product TBP $> 3 * 10^6$. (a) Linear chirp profile where the broadband spectrum is sampled uniformly. (b)Sublinear chirp profile where there are there are more wavelengths in the central part of the spectrum. (c)Superlinear chirp profile where there are there are more wavelengths on the sides of the spectrum. (d)Non-monotonic chirp profile where the mapping function between time and wavelength is non-monotonic.

by nonlinear spectrum-time-mapping can address this big data predicament by efficiently allocate more pixels to the area of interest. In Figure 2.5 (c-d), the target is illuminated by a warped spectro-temporal pattern comprising of 17 channels with a sublinear chirp profile and a chirp time of 0.56 us. As compared to the uniformly chirped source, it has the same fine frequency spacing in the central part of the spectrum and coarse spacing on the sides. The warped illumination has a lower average power and produces a central-foveated image with 43% less data. In the case where peripheral scene contains more information, a source with a superlinear chirp profile can be generated by densely sampling wavelengths on the side of the spectrum, shown in Figure 2.5 (e-f).

2.4 Time-stretch foveated LiDAR based on FDML laser

For the second implementation of our time-stretch LiDAR, we utilized a FDML MOPA laser [31, 32], centered at 1060nm (see Methods) to produce a wavelength-swept quasi-continuous wave 10nm wavelength sweep at 0.342 MHz repetition rate. The output is pulse-modulated by an electro-optical modulator (EOM) at 88 MHz to produce spectro-temporal pulse trains that comprises 256 pulses with 11ns temporal interval, resulting in a giant TBP of $9 * 10^6$ and a maximum detection range of 1.7m (as shown in Figure 2.6). Because the temporal encoding is determined by the pulse modulation, one can digitally program the modulator to sample at a higher speed to achieve a high number of pixels, or at a lower speed to increase the detection range, without increasing the system complexity. Using this source, we demonstrate a time-stretch LiDAR in Figure 2.7. The same target used in the case of discrete time-stretch LiDAR is spectrally scanned in the horizontal direction at 0.342 MHz with 256 pixels per line.

2.5 Methods

In the true-time delay method, a fiber-based gain-switched supercontinuum laser (YSL Photonics) generates broadband pulses with 300ps FWHM at 1MHz which are demultiplexed to discrete spectral channels 50GHz spacing covering wavelength from 1530nm-1560nm by a photonic-lightwave-circuit based arrayed waveguide grating (NTT Electronics Corporation). The wavelength-dependent true-time delay are provided by single-mode fibers that with 7m incremental length difference (customized by Haiyu Optics Corp. Shenzhen, 0.14dB/km attenuation). The pulse trains are amplified by erbium-doped amplifier (IPG Photonics EAD-200CL) by 1000 times to provide high instantaneous intensity for remote sensing. The spectro-temporal source is collimated and dispersed by a grating (Spectrogon) with 1100 line/mm frequency at a diffraction angle of 83°. Thanks to the matured optical communication market, wavelength multiplexing with 1000 channels and 10GHz spacing is available [33],

which permit LiDAR imaging with high angular resolution and high pixel number. Unlike the conventional time stretch that relies on the dispersion property of DCFs which operates at 1550nm only, the discrete time stretch is based on true time delay and can be applied to a broad wavelength. As a proof-of-concept demonstration, we apply the idea to lifetime imaging where the spectro-temporal pattern center at 620nm provides non-mechanical line scanning for fluorescent imaging(see Figure 2.8).

The second implementation consists of a FDML-MOPA laser center at 1060nm and high-speed EO modulation, similar to described earlier [32]. The FDML laser provides a combination of large spectral span along with microseconds time span and narrow instantaneous linewidth. This novel type of laser has mainly been used for various imaging modalities at different operation wavelength [34,35]. The wavelength sweep is accomplished by a fiber Fabry-Perot-Filter (Lambdaquest) driven at 171kHz. The FDML output is two-times buffered to 342 kHz sweep rate. After the buffer stage, a booster semiconductor optical amplifier (SOA, Innolume SOA-1060-90-Hi-30dB) was installed. The electronic waveforms for the filter and the 50% modulation of the cavity SOA (same model as in booster stage, driven by a Highland Technologies T160 driver) were programmed on an arbitrary waveform generator (Tektronix AWG7052). The electronic pulses were obtained by differentiating the digital marker outputs of the AWG using a 2.92mm step-to-impulse converter (Entegra Corp.). The obtained optical pulse length was measured to be 65ps. As amplitude electro-optical modulator (EOM) a 20GHz bandwidth model (Photline NIR-MX-LN-20) was employed in combination with an electronic pulse amplifier (Multilink MTC5515). The optical pulses were amplified by home-built ytterbium-doped fiber amplifiers (YDFAs) consisting of three-stages, two core-pumped and one cladding pumped YDFA at 976nm. Upon exiting the single-mode fiber, the light was collimated and incident on a grating with 1200 lines/mm resolution and positioned at a 30°angle. A beam expander comprises of a 250mm lens and a 50mm lens can be used to compress the beam size and enlarge the scanning angle by 5 times. The vertical illumination is achieved with a galvanometric mirror (EOPC Corp.) that scans at 2kHz.

2.6 Discussion

In this study, we propose the time-stretch foveated LiDAR and demonstrate two different implementations of it for inertia-free LiDAR imaging in one dimension with ∼MHz line rate, high resolution, and adaptive visions which uses a spectro-temporal encoded laser source and a single pixel detector. The concept is demonstrated with two different implementations that are based on two different methods for spectral-temporal encoding through discrete time-stretch. The true-time delay method spectrally samples a broadband pulse and assigns each pulse with a wavelength-dependent true time delay. The FDML method temporally samples a chirped quasi-continuous wave source. Both configurations produce tens of nanometer sweeping bandwidth, repetition rate of ∼MHz, a giant TBP of over 10^6, and tunable non-uniform spectral sampling for foveated imaging. The two techniques can be employed at a broad operating wavelength, permitting one to choose between the near-infrared band where there are matured silicon-based imaging sensors and the mid-infrared wavelengths which are safer to human eyes. They are both fiber-based and can meet the requirements on footprint and robustness of consumed-based applications. See the comparison between the proposed time-stretch methods with the conventional continuous time-stretch methods that are based on dispersive media in Table 2.1.

As compared to the true-time delay method where the physical connections inside the RPF

Table 2.1: Comparison between time-stretch methods

	Methods	Chirp	Delay	TBP	Tunability	Loss
Discrete	True-time delay	±33ns/nm	1000ns	$3 * 10^6$	<5000ns/nm	5-10dB
	FDML	±290ns/nm	2900ns	$9 * 10^6$	No	N/A
Continuous	DCF(23km)	-0.8ns/nm	25ns	$7 * 10^4$	No	10dB
	SMF(28km)	0.2ns/nm	15ns	$5 * 10^4$	No	10dB
	CMD(20m) [27]	±0.1ns/nm	2ns	7500	<0.2ns/nm	2dB
	Chirped FBG(10m) [26]	±2ns/nm	10ns	8750	<1ns/nm	4dB

scales up with the pixel number, the FDML method can be digitally programmed to gen-

erate a high number of channels without increasing the system complexity. The advantages also come with drawbacks. 1. wavelength-swept sources with a large bandwidth are usually costly. 2. It has a fixed chirp profile as restricted by the oscillation of the resonator in the laser cavity. So when the central-foveated spectral-temporal pattern is generated by densely sampling the central part of spectrum, the minimum temporal interval also shrinks, reducing the maximum detection range. On contrast, the true-time delay method is able to produce arbitrary chirp profiles and provide target-specific warped illumination without sacrificing the detection range.

The idea behind spectral-temporal encoding can be extended to achieve the inertia-free imaging in two dimensions. One solution for scanning in the second dimension is to add a second grating with a different resolution and orthogonal groove orientation [6]. The other solution is parallel illumination with delayed copies of the spectral-temporally encoded source. See the configuration of the inertia-free two-dimensional scanning in Figure 2.8.

Two of the major bottlenecks of today's LiDAR are the slow and non-robust mechanical scanning and the limited detection range. While time stretch LiDAR provide a novel approach inertia-free imaging, it can be combined with the recently proposed optical dynamic range compression (ODRC) to extends the detection range [36]. In LiDAR systems, power of the returned signal decays quadratically with the distance. To capture signals reflected from both close and remote objects, detection system with a high dynamic range is required, which is unfortunately not easily feasible at high speed. ODRC compresses the dynamic range of the returned signals by reshaping the signal through a logarithmic transformation whose decreases as the signal amplitude increases. The major disadvantage of this powerful idea is that the number of ODRC units scales with the number of detectors. While LiDAR equipped with high resolution image sensors are not good candidates for ODRC, time-stretch LiDAR which requires only a single pixel detector is a perfect match.

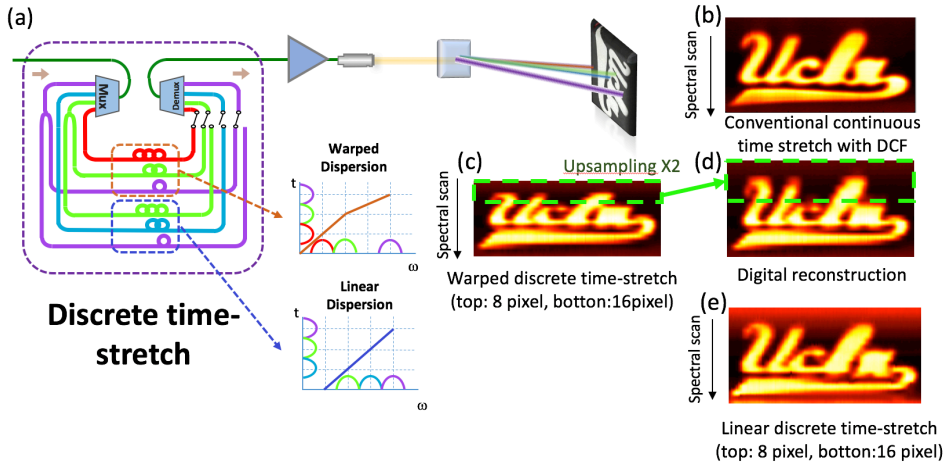

Figure 2.4: Discrete time stretch that based on the true-time delay method enables a foveated (warped) imaging in STEAM system. As compared to the conventional time stretch where the chirp comes from material dispersion of the DCF fiber, the discrete time stretch enables a target-specific non-uniform illumination that reduces the massive amount of data generated in high-speed imaging. It can also compensate for the nonlinear diffraction caused by the grating to provide a linear space-to-wavelength-to time mapping, which is not possible in conventional time-stretch systems and requires post-processing digitally. (a) The broadband pulse from a mode-locked laser centered at 1550nm with a repitition rate of 30MHz is non-linearly sampled in spectrum and assigned a wavelength-dependent true-time delay that has a warped (orange) or linear (blue) chirp profile. The generated signal is diffracted in the horizontal direction to provide illumination for the target. The spatial reflectivity information is encoded onto the returned signal and detected with signle pixel detection (not shown). (b) Conventional time-stretch imaging is only able to provide a fixed sampling pattern along the direction of spectrum scan. (c)Discrete time-stretch provides imaging with a warped sampling pattern. The top part is illuminated with a half amount of sampling beams and 2 times less data is generated as compared to the linear case. (d)The top part of the target is recovered by digital upsampling of 2 times. Artifiects on the edge is caused by the optical data compression. (e) Discrete time-stretch imaging with a linear chirp profile achieves the same imaging quality as the conventional time-stretch imaging with DCF fibers.

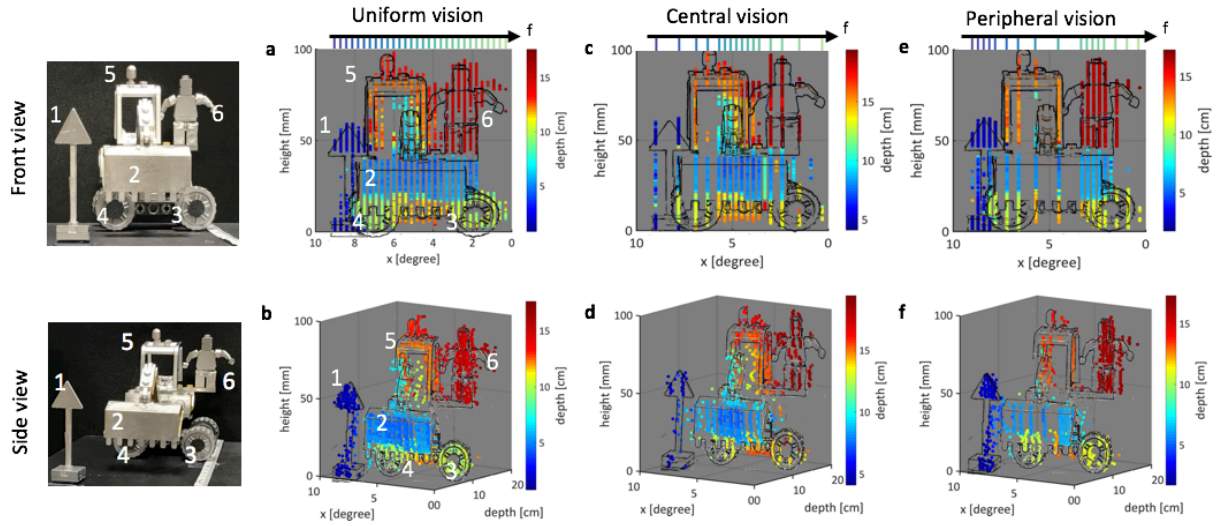

Figure 2.5: LiDAR based on true-time delay permits inertia-free imaging in one dimension with an adaptive foveated vision and optical compression. The pulse trains generated with discrete time stretch are diffracted in free space to provide spectro-temporal-encoded line illumination in the horizontal direction. It achieves ultrafast LiDAR imaging at 1 million lines per second with a maximum detection range of 5m and a field-of-view of 6°. By using a warped illumination, a foveated imaging can be generated to compress the massive amount of data generated at such high imaging speed as well as bring down the average illumination power. The target is a Lego toy (H*W*D: 10cm*10cm*20cm) positioned 1m away. The LiDAR imaging of a Lego toy with (a-b), a uniform vision with 30 pixels per row with equally spaced samples, (c-d), a foveated vision with 17 pixels per row where more samples are in the central region, (e-f), a foveated vision with 17 pixels per row where more samples are in the peripheral region.

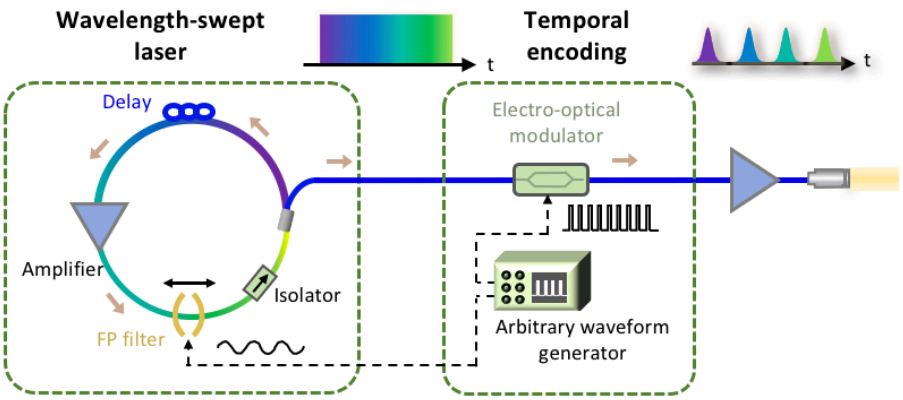

Figure 2.6: Implementation 2 with the FDML laser. It generates the spectro-temporal pulse trains with a giant TBP and digitally programmable temporal encoding. A wavelength-swept FDML MOPA source that is based on the frequency-domain mode locking laser generates a chirped quasi-continuous wave. It is sampled by an electro-optical modulator that is driven by an arbitrary waveform generator to produce spectro-temporal-encodes pulse trains. The output is amplified to compensate the loss during the modulation. Because the temporal encoding is determined by the pulse modulation, one can digitally program the modulator to sample at a higher speed to achieve a high number of pixels, or at a lower speed to increase the detection range, without increasing the system complexity.

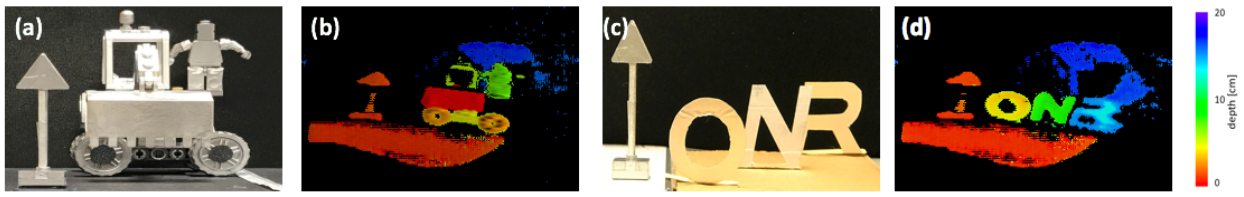

Figure 2.7: LiDAR based on the FDML laser achieves inertia-free imaging in one dimension with a high number of pixels and flexible imaging parameters. The temporal-encoded wavelength sweeping method generates a large number of spectro-temporal pulses at a repetition rate of 0.342 MHz to provide inertia-free scanning in the horizontal direction for LiDAR imaging. Two different targets positioned 1m away from the LiDAR is spectrally scanned in the horizontal direction at 0.342 MHz with 256 pixels per line. The vertical direction is scanned mechanically.

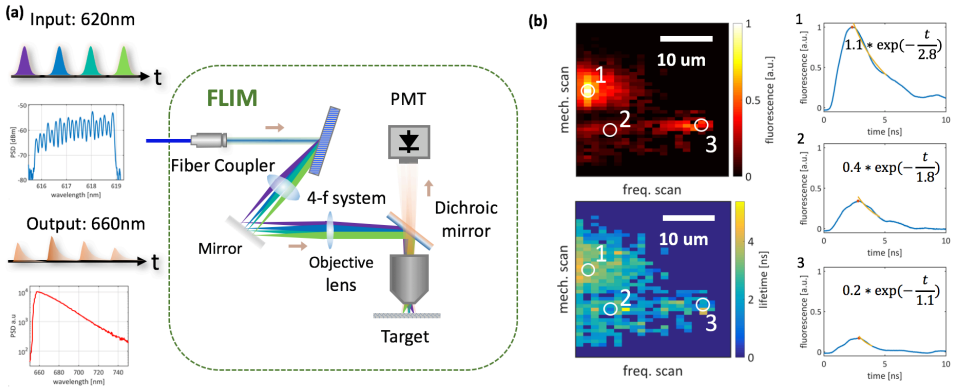

Figure 2.8: Unlike the conventional time stretch that relies on the dispersion property of DCFs which operates in mid-infrared only, the discrete time stretch is based on true time delay and can be applied to a broad wavelength. (a) As a proof-of-concept demonstration, we apply the idea to fluorescent lifetime imaging. The gain-switch supercontinuum laser generates pulse centered at 620nm, which is modulated via the true-time delay method to a pulse train comprising of 20 spectral-temporal pulses which has 0.1nm bandwidth and 300ps temporal width. The signal is diffracted to collimated beams at different angles, expanded by a 4-f system (f_1=50mm, f_2=250 mm), and focused through a microscope objective, providing line excitation for the sample (FluoSphere^{TM} Polystyrene Microspheres, 15 μm, crimson fluorescent). The fluorescent signals centered at 660nm pass a dichroic mirror and are detected by a PMT. (b)The angular position (horizontal) is recovered through the one-to-one mapping between time window and space. The vertical direction is scanned mechanically. The fluorescence information is contained in amplitude of the pulse, and the lifetime image is retrieved from the exponential tail slope (see subset).

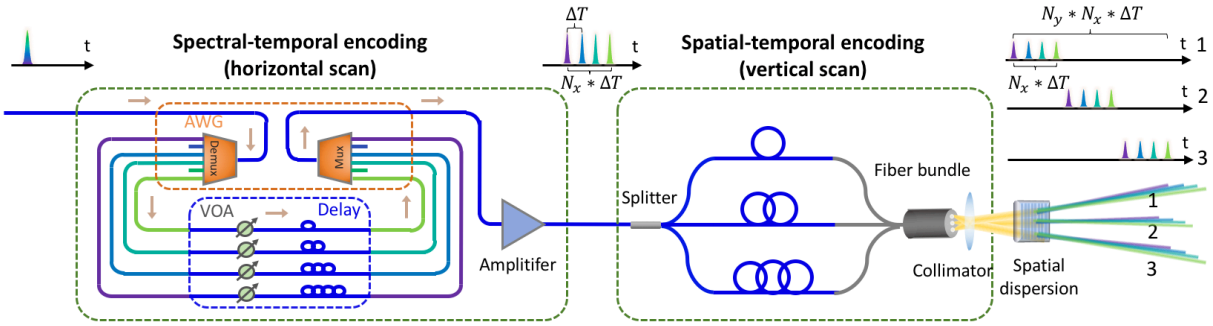

Figure 2.9: Configuration of inertia-free scanning in two dimensions using spectro-temporal encoding and spatial-temporal encoding. While spectral encoding together with spatial dispersion realize inertia-free scanning in one dimension, the spatial encoding together with fiber bundle allows temporally-encoded parallel illumination in the second dimension (vertical axis). The discrete time-stretch is shown as one way to achieve spectro-temporal encoding, where every adjacent pulse is delayed by ΔT and the total N_x wavelengths has a duration of $N_x * \Delta T$. The outputs are then spatially separated by a fiber splitter to N_y copies (with $1/N_y$ attenuation) and aligned in a row by a fiber bundle to provide parallel illumination in the vertical direction. Adjacent channels of the splitter are delayed by $N_x * \Delta T$ so that all N_y copies are concatenated in time with a duration of $N_x * N_y * \Delta T$. As every spatial location is mapped to a temporal window, a single-pixel detector rather than the sensor array is required for three-dimensional imaging, and no complicated signal processing is needed for recover the information. The frame rate is $1/(N_y * N_x * \Delta T)$. The adaptive foveated vision can be achieved by switching the connection of true time delay to the different channels of the AWG or the fiber bundle.

CHAPTER 3

Optical dynamic range compression

3.1 Introduction

A detector with a large dynamic range is desired in nearly all optical sensing and communication applications, including ranging [37], spectroscopy [38, 39], fluorescence imaging [40–43], optical coherent tomography [44], quantum optics [45], and coherent optical networks [46]. For example, in Light Detection and Ranging (LiDAR) systems, the power of the returned signal decays quadratically with the distance, so that the maximum detection range is limited by the dynamic range of the detection.

The trade-off between speed, sensitivity, and dynamic range poses fundamental challenges to the detection system. Optical amplifiers boost the lower portion of the dynamic range above the noise floor and help with the measurement of small signal amplitudes. However, it also requires the receiver to have a larger linear range and higher number of bits for quantization [7]. Optical detectors with the internal amplification (e.g. avalanche photodiodes) are used for sensitive measurements of faint light, whereas the detection speed is limited by the fundamental trade-off between gain and the bandwidth in all electronic systems [47]. While averaging reduces the effective noise and increases the sensitivity, it inevitably reduces the speed.

Photonic hardware accelerators are analog optical processors that promise to alleviate bottlenecks associated with the digital acquisition and processing of optical data [30,48,49]. One example is the amplified photonic time-stretch technology that performs the optical analog slow-motion processing and overcomes the speed-sensitivity trade-off in time-resolved single-shot measurements [3]. Here we propose another type of photonic hardware accelerator -

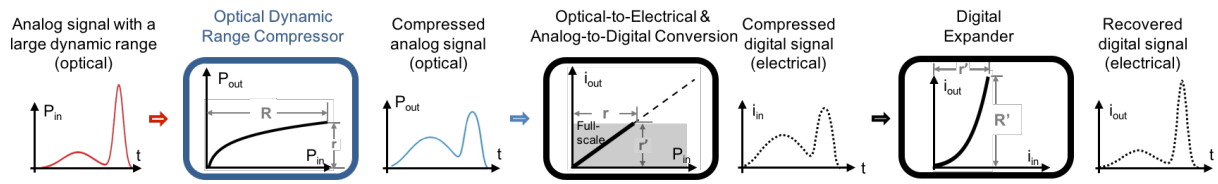

Figure 3.1: Diagram of the Optical Dynamic Range Compression. The dynamic range of the input optical signal is compressed in the optical dynamic range compressor, whose gain changes dynamically as a logarithmic-like function of the instantaneous input power. After the optical-to-electrical conversion by the photoreceiver and the analog-to-digital-conversion by the digitizer, the compressed signal is recovered through the digital expander whose response is the inverse of that of the optical compressor.

the optical dynamic range compressor (ODRC). It is a new optical signal processing method that tackles the trade-off between sensitivity and dynamic range in high-speed optical signal detection. This relieves the requirement on the dynamic range of the photoreceiver and the number of bit of analog-to-digital converters (ADCs). The concept is illustrated in Figure 3.1. The analog optical signal is first reshaped by the optical dynamic range compressor through the logarithmic-like transform. The optical transformation reduces the large dynamic range of the input to match that of the detecting system. After the optical-to-electrical and the analog-to-digital conversion, the compressed digital signal is recovered through the digital expander whose response is the inverse function of that of the optical compressor. Without requiring an optical receiver with a larger dynamic range or more quantization bits, the detectable range is extended. The chapter is arranged as follows. First, we explain the improvements on the detection sensitivity in the presence of different types of noises. Then, we show the impact of ODRC on signal statistics and LiDAR systems. Finally, we discuss the realization of ODRC and demonstrate transform profiles changing from smooth compression to sharp compression by exploring the nonlinear propagation in nano-scale silicon waveguides.

3.2 Improvement of detection sensitivity

The dynamic range of a detecting system is the difference between the smallest and the largest signal value (full-scale) it can measure. The smallest measurable signal is determined by the signal-independent noises in the detection, such as the thermal noise, dark noise and quantization noise (for quantization, the peak signal is matched to the full-scale of the ADC). The largest measurable signal is limited by the saturation of the photodiode during the optical-to-electrical conversion and the clipping by the quantizer during the analog-to-digital conversion.

3.2.1 Dynamic range limits

We now discuss the dynamic range limits imposed by the photodiode, optical amplifier, and quantizer in the high-speed optical signal detection. The ratio between the saturation limit and the input-referred noise floor depicts the dynamic range of a photoreceiver [50]. In detecting very weak inputs, the inevitable noise that originates from the thermal motion of electrons in the load resistor dominates the receiver performance (assuming photodiodes with a low dark current). At high level optical input, the output of a photodiode begins to deviate from the linear response, as evidenced by a reduction in the output current and by a diminished bandwidth. This is primarily attributed to the space-charge effect that leads to the reduction in carrier velocities and a corresponding build-up of carriers [51, 52]. A linear optical amplifier is able to boost the signal above the thermal noise of the photoreceiver and improve the sensitivity. Optical amplifiers are used when the receiver is thermal noise limited. On the other hand, since the maximum level is also increased by the same ratio, the upper range of the signal will exceed the detector saturation and the dynamic range of the ADC. The most significant challenge with optical measurements is the trade-off between the dynamic range (measured in the effective number of bits) and the speed of the ADC [1, 2, 53, 54]. While the thermal noise is the major limit at low speeds, the ambiguity caused by the limited gain bandwidth of transistors and the clock jitter becomes the dominant limitation at high frequencies. ODRC can mitigate the burden on the saturation of photodetectors and

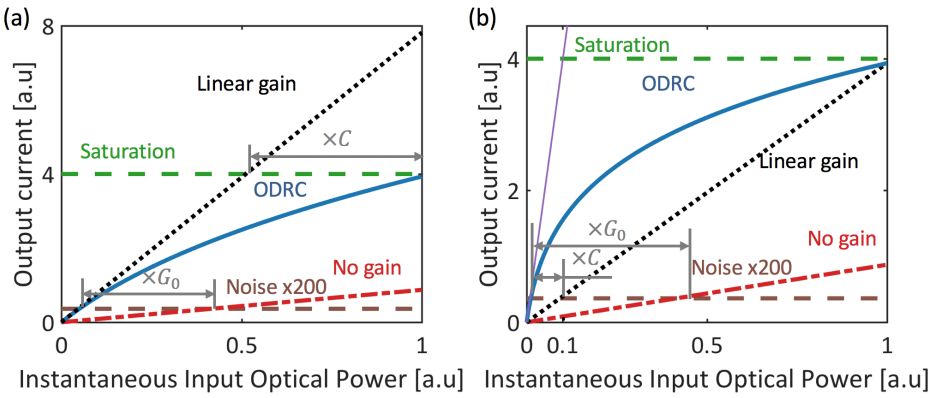

Figure 3.2: ODRC mitigates the burden on the dynamic range of the detection system. The signal-independent detection noise (brown dashed line), such as the thermal noise, dark noise, and quantization noise determines the minimum measurable signal. The saturation of the photodiode and the ADC (green dashed line) determine the maximum input. Linear amplifier (black dotted line) boosts the signal above the noise level with the unwanted effect of a smaller maximum input. ODRC (blue solid curve) tackles the trade-off by providing a logarithmic-type gain that decreases as the instantaneous input optical power increases. (a) As compared to a linear amplifier with same small signal gain G_0, ODRC compresses the upper range. The maximum input level is increased by a ratio of the compression factor $C = 2$. (b) As compared to a linear amplifier with same gain at the maximum input level, ODRC provides a higher gain for the lower range (the small gain is shown as the purple thin line). The detection sensitivity is improved by a ratio of the compression factor C=10. The logarithmic-type compression is obtained using the nonlinear propagation in silicon with nonlinear losses and saturated Raman amplification. Similar behavior can be achieved with other types of amplifiers (with fast gain response) (see Figure 3.7).

the dynamic range of the ADCs. It provides a gain that decreases as the signal amplitude increases, improving the detection sensitivity without saturating the full-scale, as shown in Figure 3.2. The output signal P_{out} after ODRC can be written as:

$$P_{out} = g(P_{in}) \cdot P_{in} \tag{3.1}$$

Here is the logarithmic-like gain of the input signal . Here, P_{out} is a monotonically-increasing concave function of P_{in}. The small signal gain G_0 is calculated as,

$$G_0 = \lim_{P_{in} \to 0} \frac{P_{out}}{P_{in}} = g(0) \tag{3.2}$$

And the compression ratio at input is defined as the ratio between the small signal gain and the gain at input P_{in},

$$C(P_{in}) = \frac{G_0}{g(P_{in})} \tag{3.3}$$

The compression ratio depicts the curvature of the sublinear gain profile. The larger it is the more compression the signal undergoes.

3.2.2 Improvement over ADC quantization noise

Performing ODRC on the optical signal before the photodetection and A/D conversion leads to the non-uniform quantization where quantization step increases as a function of the input signal amplitude. This highly desired transformation is shown in Figure 3.3. Compared to the linear case, the lower portion of the dynamic range is quantized with higher resolution, at the expense of the accuracy of the upper portion. The latter is acceptable because the impact of quantization noise is much more severe at low signal levels. The mean square quantization error or quantization noise power of an ideal ADC is calculated as [55, 56]:

$$\sigma_q^2 = E[(x - Q(x))^2] = \int_{-\infty}^{\infty} (x - Q(x))^2 p(x) dx = \sum_{k=1}^{2^n} \int_{b_{k-1}}^{b_k} (x - y_k)^2 p(x) dx \tag{3.4}$$

where x is the input signal,$Q :\rightarrow y_k, \forall x \in [b_{k-1}, b_k)$ is the mapping function of quantization,$p(x)$ is the probability density function of the input x, and n is the nominal number of the bits of the ADC. When the quantization step $\Delta_k = b_k - b_{k-1}$ is small enough and the threshold

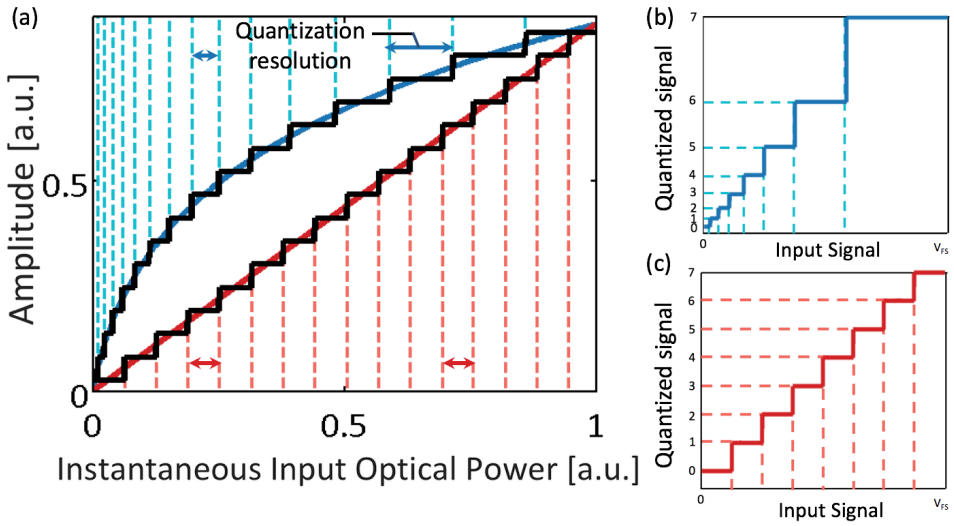

Figure 3.3: ODRC enables the non-uniform quantization where the quantization step increases as a function of the input signal amplitude. Compared to the linear case, the lower part of the dynamic range is associated with the finer quantization resolution, at the expense of the accuracy of the upper part. The latter is acceptable because the impact of quantization noise is much more severe at low signal levels. (a) The photocurrent in the case of ODRC (blue) and linear (red) transformation is quantized with a uniform ADC (black). Quantization steps are illustrated in dashed vertical lines. The mapping between the analog input signal to the quantized digital output, in the case of (b) ODRC, and (c) linear transformation. In (b), the quantized signal is recovered through the digital expander whose response is the inverse of that of the optical compressor.

value is set as the median of the bin $y_k = (b_{k-1} + b_k)/2$, (3.4) can be approximated as:

$$\sigma_q^2 \approx \sum_{k=1}^{2^n} \int_{-\frac{\Delta_k}{2}}^{\frac{\Delta_k}{2}} x^2 p(x) \approx \frac{1}{12} \sum_{k=1}^{2^n} \Delta_k^2 \cdot Pr(P_{in}) \tag{3.5}$$

where $Pr(p_{in}) = \int_{b_{k-1}}^{b_k} (x - y_k)^2 p(x) dx$ is the probability of the input falling in a given quantization bin. In the case of a uniform quantizer, the quantization resolution is a function of the full-scale V_{FS} and the nominal number of bits, n, and is independent of signal's instantaneous amplitudes,

$$\Delta_{linear} = \frac{V_{FS}}{2^n} \tag{3.6}$$

When the probability of the input falling in each interval is the same, a uniform quantizer minimizes the quantization noise power. Inserting (3.6) into (3.5) results in the well-known equation for the quantization error,

$$\sigma_q^2 = \frac{\Delta_{linear}^2}{12} \tag{3.7}$$

ADC's dynamic range is defined as the ratio of its full-scale range to the minimum resolvable change in signal. For a linear quantizer, it is proportional to the bit number n:

$$DR_{ADC}[dB] = 20log(\frac{V_{FS}}{\Delta_{linear}}) = 6.02n \tag{3.8}$$

Note that (3.8) differs from the formulation of the ADC's SNR equation by 1.76 dB, since the latter is in terms of root-mean-square values whereas the former is for peak-to-peak amplitudes. When detecting inputs with a large dynamic range, one needs to determine the proper balance between the large amplitudes, which exceed ADC's full-scale, and the small amplitudes, which get lost in quantization noise. ODRC tackles this trade-off by boosting the small amplitude without exceeding the full-scale. The quantization resolution is a function of the input amplitude:

$$\Delta_{ODRC}(P_{in}) = \frac{\Delta_{linear}}{dP_{out}/dP_{in}} = \frac{V_{FS}/2^n}{g'(P_{in}) * P_{in} + g(P_{in})} \tag{3.9}$$

The dynamic range enhancement of an ADC is:

$$DR_{ADC}[dB] = 20log(\frac{V_{FS} * C(P_{max})}{\Delta_{linear}}) = 6.02n + 20log(C(P_{max})) \tag{3.10}$$

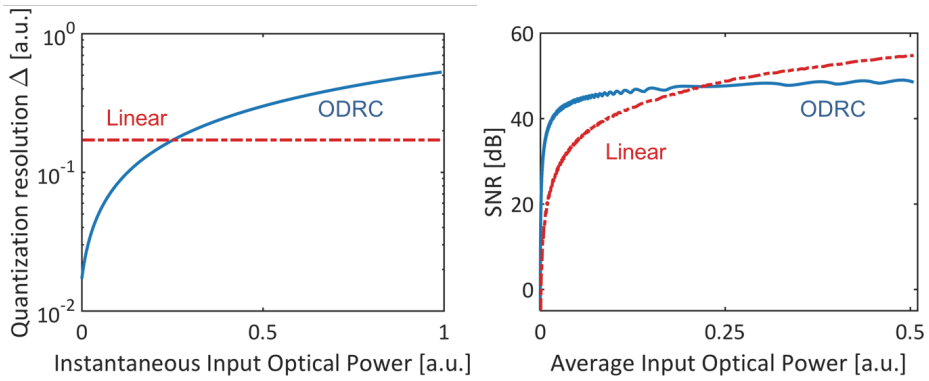

Figure 3.4: ODRC reshapes the quantization noise. The lower portion of the dynamic range is quantized with less noise and better SNR, at the expense of decreased SNR at the higher portion. (a) The quantization resolution as a function of the input amplitude. (b) Signal-to-quantization-noise ratio of quantizing a single-tone input with an 8-bit linear ADC. (The full-scale of the ADC is matched to the maximum input peak). As compared to the case of the linear quantization (red dot-dashed curve), where the SNR falls rapidly for small amplitudes, ODRC (blue solid curve) is able to provide good SNR over a wide range of signal powers. ODRC that is considered here has a compression factor C=10.

Therefore, the dynamic range is improved by $20log(C(P_{max}))$, where $C(P_{max})$ is the compression factor that is evaluated at the maximum input P_{max} which doesn't saturate the full-scale.

The reshaping of quantization noise is shown in Figure 3.4. The lower portion of the dynamic range is quantized with smaller noise, resulting in a higher signal-to-noise ratio (SNR). This is obtained at the expense of a decreased SNR at the higher portion of the dynamic range. As compared to the case in the linear quantization, where the SNR falls rapidly for small amplitudes, ODRC is able to provide the good SNR over a wide range of signal levels. Inserting (3.9) into (3.5), the mean square quantization error is calculated as:

$$\sigma_q^2 \approx \frac{1}{12}\sum_{k=1}^{2^n}\left(\frac{V_{FS}/2^n}{g'(P_{in}) * P_{in} + g(P_{in})}\right)^2 Pr(P_{in}) \tag{3.11}$$

Given the signal statistics described by its probability distribution function $Pr(P_{in})$, there exists the optimal nonlinear transform $g(P_{in})$ that minimizes the expectation of the quantization error. To achieve the same digital SNR, the signal that is optically compressed

requires fewer bits than otherwise required by a linear converter. This powerful idea enables the non-uniform quantization and data compression to be performed in the optical domain. For input signals with a non-stationary probability distribution, the sublinear transform of the optical compressor can be dynamically adapted to the histogram of the input amplitudes. The idea can be applied to smart sensing, providing flexible solutions to meet the requirements on the resolution and the accuracy in optical detections and analog-to-digital conversions.

3.2.3 Extending detection range of LiDAR

LiDAR systems measure the distance and velocity of targets by illuminating the target and measuring the time-of-flight and Doppler shift of the reflected light. The power of the returned signal decays quadratically with the distance. As a result, the maximum detection range is limited by the dynamic range of the detection and the analog-to-digital converter, characterized by the digitizer's effective number of bits (ENOB). Thus high-resolution (high-ENOB) ADCs are required in LiDAR system to achieve a large detection range. In the meantime, the depth accuracy of the system is limited by the sampling speed of the digitizer that decreases with ENOB.

ODRC extends the detection range of LiDAR systems by assigning more quantization bits (improving ENOB) for weak signals and lowering the minimum returned power the ADC can quantize, as shown in Figure 3.5. As compared to the linear case, the SNR for detecting distant targets is increased. The maximum detection range, which scales quadratically with the measured amplitude, is improved by the square root of the compression factor, $\sqrt{C}$.

3.2.4 Shaping signal statistics

ODRC redistributes statistics of a signal. By amplifying small amplitudes and compressing large amplitudes, ODRC causes a relative compression in the right side of the distribution

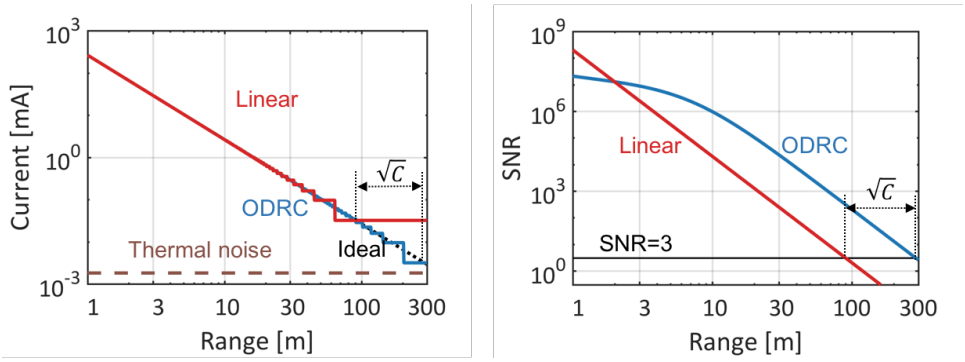

Figure 3.5: ODRC extends the detection range of LiDAR. Weak signals from distant targets are quantized with finer steps after reshaping by ODRC. The maximum detection range, which scales quadratically with the measured amplitude, is improved by the square root of the compression factor $sqrtC$.

with a concomitant suppression of outlier events.

While the Gaussian distribution is widely used to model noise in optical systems, the extreme-value statistics that studies the rare events has drawn much attention in the past decade [15, 57, 58]. In stimulated Raman amplification, extreme-value behaviors arise due to the interplay of pump laser fluctuations with the exponential transfer function of the Raman process. Studies have shown that the amplified Stokes signal has a heavy-tailed distribution [15]. The effect of ODRC on the extreme-value statistics is shown in Figure 3.6. ODRC compresses the heavy tail in the high-value region and mitigates the burden on the receiving system for detecting high-dynamic-range inputs, facilitating the study of extreme events in nonlinear optical systems.

Optical dynamic range compression may reduce the nonlinear phase noise (NLPN). NLPN is caused by the interaction of amplitude fluctuations, such as amplified spontaneous noise (ASE) and relative intensity noise (RIN), with self-phase modulation (SPM). By suppressing large-amplitude events in the probability distribution, ODRC can reduce the nonlinear phase noise.

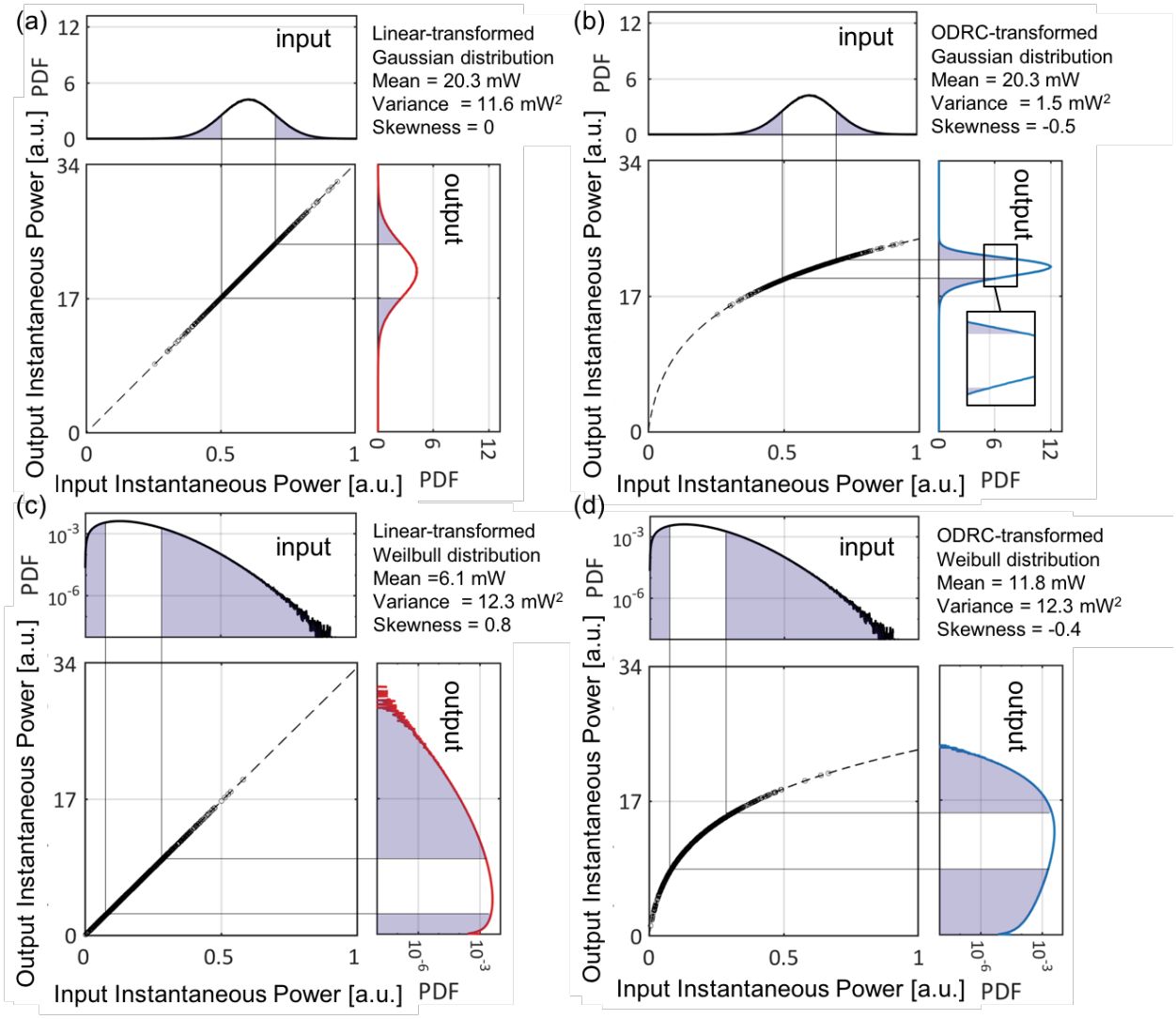

Figure 3.6: ODRC reshapes signal statistics including noise characteristics. (a)(b) ODRC reshapes the statistics of a Gaussian-distributed signal. As compared to a linear amplifier with the same average gain, it reduces the variance and the skewness of the signal (as shown by the asymmetric distribution in the subset), resulting in improved SNR. (c)(d) ODRC reshapes the statistics of a signal that follows the extreme-value distribution, shown in the logarithmic scale here. As compared to the linear amplifier that preserves the shape of the distribution, ODRC reduces the requirement for a large dynamic range in optical detection and A/D conversion stages of a receiver.

3.3 Physical realization of ODRC

Owing to the logarithmic current-to-voltage transfer characteristic inherent in PN-junctions, logarithmic compressors are widely implemented in electronics. They are used in radar and radio applications to compress the high dynamic range of received signals at MHz. Due to the lack of logarithmic behaviors in optics, implementing such powerful techniques optically has not been possible.

Recently, an optical method to create the logarithmic function was introduced. The saturated amplification and nonlinear absorption in a silicon photonics waveguide were tailored to approximate a logarithmic function with an input range of up to 19.5dB. The optical logarithm was shown to perform optical exponentiation and signal deconvolution [59–61]. This opens one possible path to realize the dynamic range compression optically. Fortunately, an exact logarithmic behavior is not needed for ODRC, making the implementation easier.

Various approaches for the experimental realization of ODRC are illustrated in Figure 3.7. To compress the high-dynamic-range-optical signals in high-speed detection, ODRC devices should have a nonlinear gain/loss that decreases/increases as input amplitudes increase, and is able to respond to the instantaneous power change.

Saturated amplifiers can be used to shape input amplitudes by providing a higher gain for small inputs, and a lower gain for large inputs as the pump is depleted. This behavior can be tuned by changing the pump power. A stronger pump leads to a larger compression ratio. Amplifiers with ion-doped gain medium such as erbium-doped fiber amplifier (EDFA) and ytterbium-doped fiber amplifier (YDFA) have gain relaxation time at milliseconds owing to the long metastable lifetime. Such a long relaxation time is preferable for low noise, but also limits the device's response time. Semiconductor optical amplifiers (SOA), on the other hand, have a much shorter upper state lifetime of few nanoseconds. Saturated SOAs can also be used to compress signals. The lifetime of SOA can be dramatically reduced to picoseconds with quantum-dot structures [62].

Raman amplification that is based on stimulated Raman scattering (SRS) is widely used in optical communications and biomedical applications for its broadband gain and low noise

performance. The response time of the Raman process is at the order of tens of femtoseconds in amorphous solids such as glasses, and a few pico-seconds in crystalline solids such as silicon [63,64]. For ODRC using Raman-pumped optical fibers of kilometers, the walk-off between the co-propagating pump and signal beams becomes the major limitation of the device bandwidth [65]. Raman amplification has a gain coefficient in silicon that is four orders larger than it is in silica [66] and it was used to realize the first silicon optical amplifier [67] and the first silicon laser [64]. Unlike the SOA, Raman amplification causes minimum phase distortions and can be used for ODRC in coherent applications.

Two-photon absorption (TPA) generates loss that increases quadratically with the input intensity and can be used to compress high amplitudes at ultrafast speed. In semiconductors like silicon, free carriers generated during TPA introduce free carrier absorption (FCA) that contributes to dynamic range compression. However, the free carriers with a long lifetime reduce the response speed [68]. Studies have also shown that TPA-induced free-carrier loss degrades the noise figure of a silicon Raman amplifier by an amount that depends on the carrier lifetime [69]. Using silicon nanowire can greatly enhance the nonlinear effect as well as increase the device bandwidth and reduce the noise figure, as the intensity increases and lifetime reduces in nanoscale waveguides [52]. Carrier sweep-out using a reverse-biased PN-junction further reduces the free-carrier lifetime to tens pico-seconds [66,70]. III-V materials, such as GaAs and InP, are also candidates for performing ODRC. They have a two-photon absorption coefficient much larger than that of silicon, and a short lifetime as a result of the direct bandgap [71, 72].

While the reverse-biased waveguide enables carrier removal and ODRC at high operation bandwidth, a forward-biased waveguide can be used to harvest the energy during the compression at the cost of device speed [73]. Here, using the two-photon photovoltaic (TPPV) effect, electric power is recycled from the photons that were lost through the compression of the high amplitudes. Energy harvesting has been achieved in silicon wavelength converters [74], modulators [75], and Raman amplifiers [76]. Such low-energy consumption devices reduce power dissipation as well as chip heating, which are of paramount importance for chip-scale integration in silicon photonics.

We demonstrate ODRC with energy harvesting by simulation the nonlinear propagation in a forward-biased nano-scale silicon waveguide, taking saturated Raman amplification, TPA, and FCA into account. Logarithmic-transform profiles with soft and sharp compression are achieved by varying the input Raman pump intensity and the bias voltage, as shown in Figure 3.8. A tunable ODRC allows one to select the optimal compression profile that matches with signal statistics, adaptively balance between the detection of small and large amplitudes, maximizing the detection SNR. ODRC devices based on nonlinear absorption has an operation wavelength limited by material bandgap. For wavelengths above 2.2um, nonlinear absorption will not be an option for compression due to the absence of TPA, and only saturated amplification can be utilized [77].

Nonlinear refraction mechanisms form another approach for the experimental realization of ODRC. In nonlinear materials, the large peaks produce changes in the refractive index that lead to an intensity-dependent loss in the transmission [78, 79]. For example, a positive/negative lens generated by the strong inputs causes the beam to self-focus/self-defocus and to be blocked by an aperture placed at the output [80]. This non-absorptive phenomenon can realize compression with a large compression factor. It can be cascaded with the saturated amplification and nonlinear absorption to construct versatile ODRC devices. The proposed methods for the experimental realization of ODRC are compared in Table 3.1.

Table 3.1: Potential implementations of ODRC

Device	Power Consumption	Speed	Compression ratio	Noise Figure	Principles	Complexity
Reverse-biased silicon nanowire with saturated Raman pump	Medium	>50 GHz[67]	Large and tunable	~5dB [68]	SRS, TPA, FCA	Medium
Optical fiber with saturated Raman pump	High	>1 GHz[64]	Large and tunable	~5dB	SRS	Medium
Saturated SOA	Medium	>1 GHz	Large and tunable	~8dB	SOA	Medium
Forward-biased silicon nanowire	Negative[44]	>0.5 GHz[67]	Medium	>3dB	TPA, FCA, TPPV	Medium
GaAs resonator	Zero	>1 GHz[77]	Medium	>3dB	TPA, FCR, FCA	Medium
Quantum-well-based optical limiter	Zero	>50 GHz[79]	Large	>3dB	Optical Kerr	High

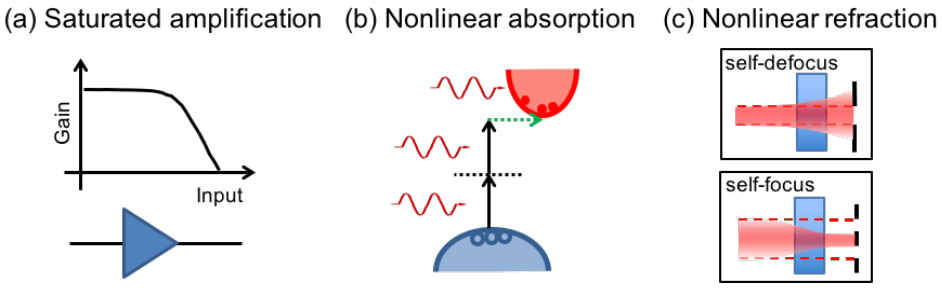

Figure 3.7: Various approaches for the experimental realization of ODRC.

3.4 Conclusion

We describe a new concept in optical signal processing that can improve the sensitivity and dynamic range, and outline several methods for its experimental realization. The nonlinear optical transformations utilized here increase the signal bandwidth, which is potentially an undesired effect. Therefore, they should be utilized only when the system is dynamic-range-limited and not bandwidth-limited. Time stretch techniques have been very successful in overcoming the bandwidth limitation in optical data acquisition and have led to spectacular successes in the discovery of new optical phenomena and creation of new class of biomedical instruments with extreme throughput15. Combining time stretch with optical data compression presents an intriguing area for research.

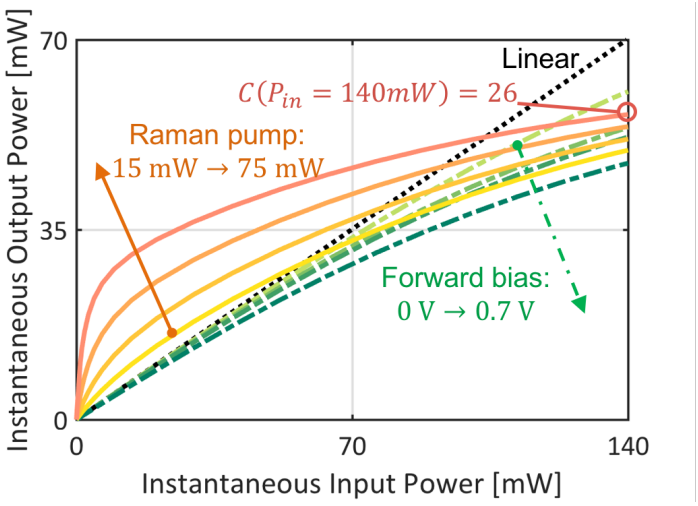

Figure 3.8: ODRC with energy harvesting is realized in a forward-biased nano-scale silicon waveguide with saturated Raman amplification. A tunable compression profile is achieved by varying Raman pump intensity and forward bias. When forward bias increases from 0V to 0.7V and Raman pump is 0mW (line's color varies from light green to dark green), more free carriers generated from TPA can accumulate in the waveguide, resulting in a more compressed output. When Raman pump increases from 15mW to 75mW and forward bias is 0.7V (line's color varies from yellow to red), gain depletes at weaker input. A sharp compression profile is realized using large Raman pump and high forward bias. The compression factor at 140mW input is 26 with 75mW Raman pump and 0.7V forward bias. (Waveguide dimension: 220nm*450nm*1cm)

CHAPTER 4

Analog optical computing primitives in silicon photonics

4.1 Introduction

With the proliferation of big data and the rapid increase in power dissipation of electronics, there is renewed interest in the use of optics for computing. In contrast to the optical computing efforts of the past, an all-optical computer may not be the most prudent goal [30, 81]. Instead, a hybrid approach where optical systems are selectively applied to alleviate bottlenecks and assist electronic processors is a more fruitful pursuit. The idea of optical co-processors is proposed as hardware accelerators to take part of the processing burden off of the electronic processors [3, 26, 29], as shown in Figure 4.1(a). Composed of carefully designed photonics components, the optical co-processor performs a certain analog computational operation in real time on the input optical signal before it is acquired and digitized. Among the analog-computing primitives, the logarithmic function is of importance and is one of the most challenging operations to perform in optics. The logarithmic primitive has broad applications, including the log-likelihood estimation for machine learning, recovery of signal with multiplicative distortion, and the exponentiation operation (raising a variable to given power). As illustrated in Figure 4.1(b), an optical implementation of the exponentiation operation can be achieved by three sequential components: the logarithmic primitive, the scaling primitive, and the natural exponentiation primitive. Apart from the logarithmic primitive, the two remaining primitives can be emulated using commercially available optical systems. For example, scaling can be achieved with variable optical attenuators or four-wave mixing, while a Raman amplifier operating in the low depletion regime provides the natural

exponentiation function with respect to the input intensity.

The lack of logarithmic dependence in conventional optical interactions renders the realization of a logarithm computation block formidable. Logarithmic filtering was demonstrated in literature using nonlinear photographic films [82] and hologram masks [83], but the cumbersome free space setup and the complicated processing have limited its range of applicability.

In this paper, we show an approach to approximate the optical input-output relationship

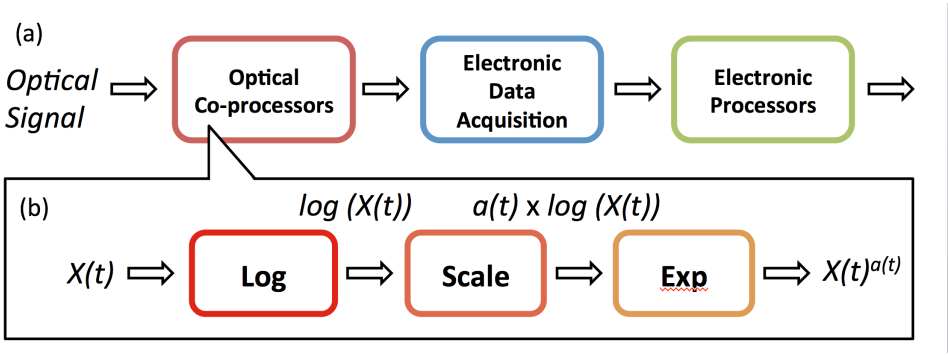

Figure 4.1: (a) Optical co-processors that perform computational operations on optical input signal can be placed before the optical-to-electrical conversion to take part of the processing burden off of the electronic processors [4]. (b) As one of the building blocks of the optical co-processors, the exponentiation operation is composed of the Logarithmic Primitive (Log), the Scaling Primitive (Scale) and the Natural Exponentiation Primitive (Exp).

as a logarithmic function in a silicon waveguide via numerical studies. Silicon naturally exhibits two-photon absorption (TPA) at telecommunication wavelengths. This nonlinear absorption, which limits the signal's output intensity and is normally deleterious [66, 67, 84], becomes a fortuitous natural candidate to approximate the logarithm. In the presence of a suitably wavelength-shifted pump source, stimulated Raman scattering amplifies the signal, and it has such a strong effect that it caused this indirect band-gap material to lase for the first time [64]. When the signal grows strong enough to deplete the pump source, the gain saturates, leading to a second method to achieve logarithm-like behavior. Non-degenerate TPA is also introduced to the system to shape the output curve. Using several effects simultaneously allows one to engineer their relative strengths, improving the dynamic range and lowering the required signal intensity.

4.2 Synthesis of optical logarithm in silicon photonics

For a quasi-continuous signal with wavelength below silicon band edge, two-photon absorption (TPA) and the induced free-carrier absorption (FCA) are the main sources of nonlinear loss in silicon waveguides. The evolution of optical intensity along the waveguide is described as [85]:

$$\frac{dI_s}{dz} = -\alpha I_s - \beta_{TPA} I_s^2 - \sigma \Delta N I_s \tag{4.1}$$

where α is the linear loss coefficient, $\beta_{TPA} = 5 * 10^{-12} m/W$ is the TPA coefficient, which is proportional to the imaginary part of third-order susceptibility, and $\sigma = 1.45 * 10^{-21} m^2$ is the cross section of free carrier absorption, at 1550 nm [85]. At steady state, the free carrier density ΔN is represented by

$$\Delta N = \frac{\tau \beta_{TPA}}{2h\nu_0} I_s^2 \tag{4.2}$$

where τ is the free carrier lifetime, and $h\nu_0$ is the photon energy. The optical limiting phenomenon is observed at high input intensity as a result of the dominant nonlinear loss [86]. Between the linear region and the saturation region, there exists a sublinear curve that resembles a logarithmic function, as illustrated in Figure 4.2. The logarithmic region is defined as the largest input intensity range whose output can be fit to a logarithmic function. As a measurement for the fitting accuracy, two deviation calculation methods are employed. To evaluate the average accuracy of the computing primitive, the normalized root-mean-square error (NRMSE) should be no larger than 1% and is defined as

$$NRMSE = \frac{\sqrt{< (I_{out} - I_{fit})^2 >}}{(I_{max} - I_{min})} \tag{4.3}$$

To ensure the accuracy of each single input value, the maximum error should be no larger than 3.5% and is defined as

$$MaxError = max(\frac{|I_{out} - I_{fit}|}{I_{out}}) \tag{4.4}$$

An example of waveguide with length Z = 2 cm, lifetime τ = 1 ns, and propagation loss

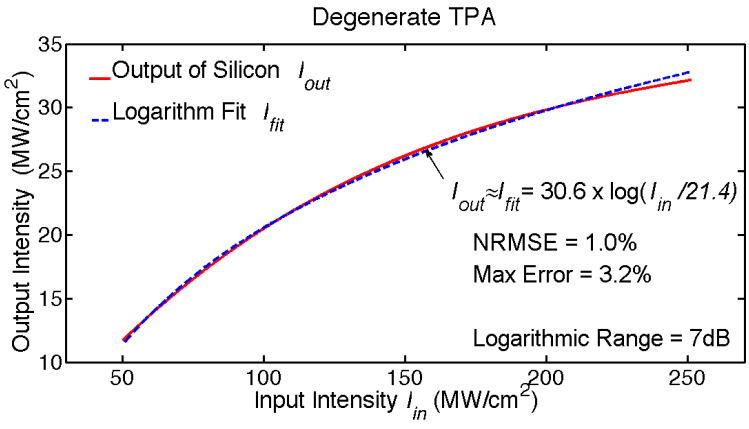

Figure 4.2: Numerical demonstration of the logarithmic computing primitive in a silicon waveguide. The signal undergoes degenerate two-photon absorption (TPA) and free-carrier absorption (FCA). The output is fit to a logarithmic function over a 7 dB input range with a normalized-mean-square error of 1.0% and the maximum error of 3.2%.

α=3 dB/cm is shown in Figure 4.2. The signal undergoes degenerate TPA and FCA and is fit to a logarithmic function I_{fit} over the input intensity range $50MW/cm^2$ to $250MW/cm^2$, resulting in 7 dB dynamic range. It is noted that it requires very high input power to reach the logarithmic region. This results from the large ratio between the linear loss coefficient and the nonlinear loss coefficient: the nonlinear term only comes into effect when input intensity is above a certain region. A low propagation loss coefficient and a large free-carrier lifetime would reduce this ratio and shift the logarithmic region to lower input intensity. Unfortunately, a large free-carrier lifetime is not practical because it also reduces device's speed, while ultra-low linear absorption is limited by the fabrication technology. A practical computing primitive thus would require larger logarithmic range, lower power, and more flexibility.

Stimulated Raman Scattering offers optical gain in silicon without requiring phase matching [87]. The saturation of Raman amplification provides the opportunity to reach the logarithmic region with low input signal power. It also increases the dynamic range without significantly increasing setup complexity.

The Raman amplification in silicon along with nonlinear absorption can be modeled as [67]:

$$\begin{cases} \frac{dI_s}{dz} = (-\alpha + g_R I_R) I_s - \beta_{TPA}(I_s + 2I_R) I_s - \sigma \Delta N I_s \\ \frac{dI_R}{dz} = (-\alpha - \frac{\lambda_s}{\lambda_R} g_R I_R) I_s - \beta_{TPA}(I_R + 2I_s) I_R - \sigma \Delta N I_R \\ \Delta N = \frac{\tau_c \beta_{TPA}}{2h\nu_0}(I_s^2 + I_R^2 + 2I_s I_R) \end{cases} \tag{4.5}$$

where $g_R = 76$cm/GW is Raman gain coefficient [8],and I_R is the Raman pump intensity. Without loss of generality, the wavelength dependence of the linear loss coefficient α, TPA coefficient β_{TPA}, and FCA coefficient σ are ignored.

At low input signal intensity, Raman pump source amplifies the output signal. The gain becomes less significant when the input signal grows, as the pump source is depleted by nonlinear absorption and amplification. Gain saturation modifies the input-output curve and expands the logarithmic region. Although it has a similar system setup, the logarithmic computing primitive functions fundamentally differently from a silicon Raman amplifier [67, 84]. In the later case, the signal intensity is significantly smaller than the pump. Under the assumption of negligible pump depletion, the output signal increases linearly with the input. In the logarithmic computing primitive case, both pump depletion and nonlinear absorption modify the output signal to be a sublinear function of the input. And unlike the case in [84] where picosecond pulse signals are considered, the proposed signal focused on quasi-steady signal, where self-phase modulation and cross-phase modulation have minimum effect.

As shown in Figure 4.3, a 10.5 dB logarithmic region for signal input from $0.035 MW/cm^2$ to $0.4 MW/cm^2$ is achieved when the input Raman pump is $91 MW/cm^2$. The introduction of the amplification significantly reduces the power requirement on the signal power, and also increases the logarithmic range.

A numerical sweep of the input pump intensity shows that at $48.5 MW/cm^2$, the input logarithmic range is further expanded to 17.5 dB, from $0.4 MW/cm^2$ to $22.4 MW/cm^2$, as shown in Figure 4.4. The Raman pump expands device flexibility, allowing one to trade between Raman pump intensity, signal intensity and logarithmic range. We also note that scaling the signal intensity before or after the logarithmic step allows one to increase or decrease the range of valid signal intensities (though we acknowledge that the dynamic range remains at best unchanged).

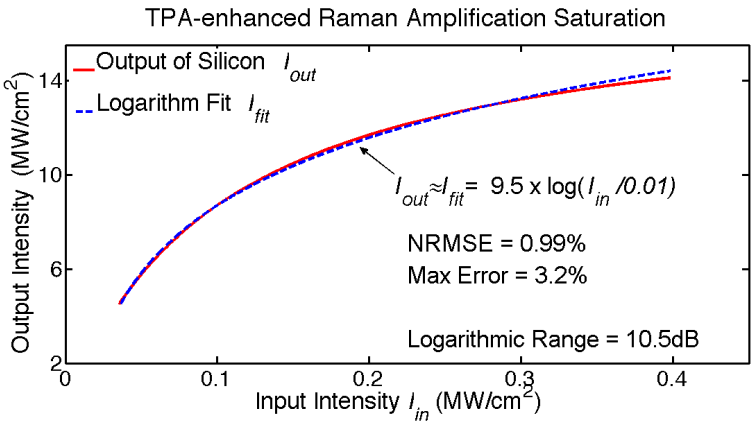

Figure 4.3: Similar to Figure 4.2, a simulation of the logarithmic computing primitive wherein Raman amplification along with concomitant non-degenerate TPA is added to increase the dynamic range and vastly reduce required signal intensity. The input Raman pump intensity is $91 MW/cm^2$. The output is fit to a logarithmic function over a 10.5 dB input range with a normalized-mean-square error of 0.99% and the maximum error of 3.2%.

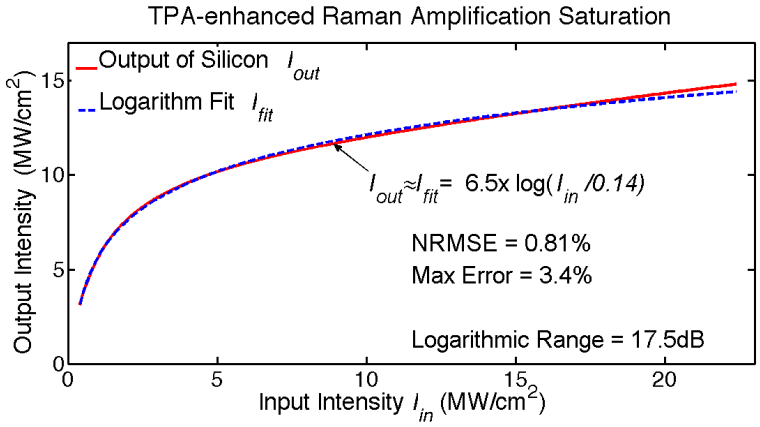

Figure 4.4: Simulation of the logarithmic computing primitive under the same conditions as in Figure 4.3 (the signal undergoes saturated Raman amplification and non-degenerate TPA) except that the input Raman pump intensity is lowered to $48.5 MW/cm^2$. Reduced Raman pump requirements and an increased logarithm dynamic range of 17.5 dB is gained at the expense of higher required signal intensity. The normalized-mean-square error is 0.81% and the maximum error is 3.4%.

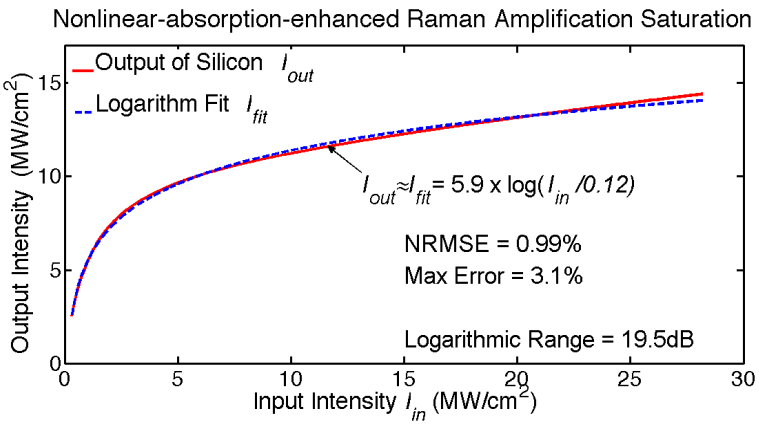

Figure 4.5: Synthesis of the logarithmic computing primitive with the nonlinear-absorption-enhanced Raman amplification. The input Raman pump is $56.1 MW/cm^2$ and the input non-degenerate TPA pump source is $50.1 MW/cm^2$. The output is fit to a logarithmic function over a 19.5 dB input range with a 0.99% normalized-mean-square error of 0.99% and a 3.1% maximum error.

Although the use of a Raman pump can immensely reduce the required signal intensity (cf. Figure 4.3 and 4.4), the output deviates from a logarithm at higher signal intensities. To shape the curve at high input intensity, a new pump source I_P is injected into the waveguide to enhance the nonlinear absorption process through non-degenerate TPA with the signal wave. The evolution of signal wave I_s, Raman pump wave I_R, and non-degenerate TPA pump wave I_P can be modeled as:

$$\begin{cases} \frac{dI_s}{dz} = (-\alpha + g_R I_R) I_s - \beta_{TPA}(I_s + 2I_R + 2I_P) I_s - \sigma \Delta N I_s \\ \frac{dI_R}{dz} = (-\alpha - \frac{\lambda_s}{\lambda_R} g_R I_R) I_s - \beta_{TPA}(I_R + 2I_s + 2I_P) I_R - \sigma \Delta N I_R \\ \frac{dI_P}{dz} = -\alpha I_P - \beta_{TPA}(I_P + 2I_s + 2I_R) I_P - \sigma \Delta N I_P \\ \Delta N = \frac{\tau_c \beta_{TPA}}{2h\nu_0}(I_s^2 + I_R^2 + I_P^2 + 2I_s I_R + 2I_s I_P + 2I_R I_P) \end{cases} \tag{4.6}$$

The non-degenerate TPA with the third beam I_P suppresses the output signal as the input increases, extending the logarithmic range at the high-input side. For input Raman pump I_R at $56.1 MW/cm^2$ and the input non-degenerate TPA pump source I_P at $50.1 MW/cm^2$, the logarithmic input range is enlarged to 19.5 dB, from $0.32 MW/cm^2$ to $28.2 MW/cm^2$, as shown in Figure 4.5. Note that the optimized initial pump intensity varies with wavelength

due to the nonlinear coefficient's dependence.

4.3 Application to optical computing

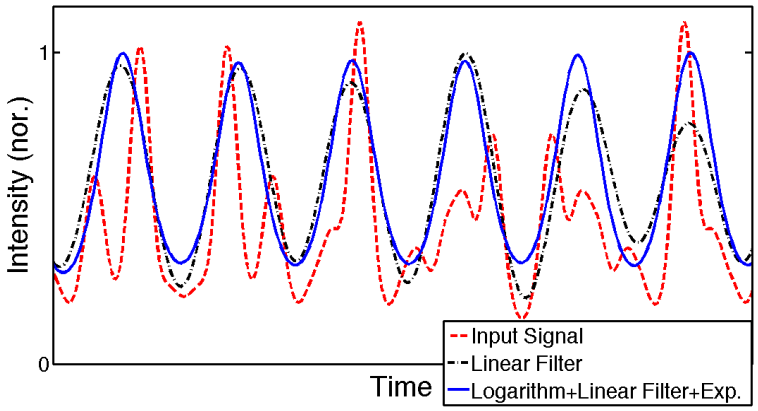

Figure 4.6: The silicon photonic logarithm device can perform signal de-convolution. It can be used to recover a signal of interest when it has been mixed (multiplied) by unwanted signal of different frequencies. The Figure shows the composite signal (dashed red) consisting of a single tone input mixed with two unwanted higher frequency tones. Linear filtering (dashed dot black) is unable to recover the input. Logarithm followed by linear filter (and natural exponentiation) is able to recover the input (solid blue). In both cases the linear filter is a 10th order Butterworth.

One important application of the silicon photonic logarithmic device is for recovery of a signal of interest in the presence of multiplicative distortion [61]. This technique exploits the fact that the logarithm of the product of two inputs is the sum of the logarithms of those inputs. This allows ones to filter multiplicative noise by logarithmic filtering and conventional linear time-invariant filtering. Figure 4.6 illustrates this application. As explained in the caption, the logarithm device followed by a linear filter can de-convolve and recover the signal from a mixed composite.

Compared to the synthesis of the logarithmic computing primitive, the scaling and the natural exponentiation computing primitive are implemented in a more straightforward way.

One way to perform the scaling function is to use a variable optical attenuator. A p-i-n diode structure fabricated on Si waveguide attenuates the input optical beams as a function of the current injection density [88, 89].

Another way to implement the scaling primitive is to use the third-order parametric process. The output wave at a new frequency wave ω_4 is generated from the mixing of the input waves at ω_1,ω_2, and ω_3 as [90]:

$$\frac{dE_4}{dz} = \frac{-\alpha}{2}E_4 + i\frac{2n_2\omega_4}{c}E_1E_2E_3^*e^{-i\Delta kz} \tag{4.7}$$

$$\rightarrow \frac{dI_4}{dz} = -\alpha I_4 + \frac{2n_2\omega_4}{c^2\epsilon_0 n}\sqrt{I_1I_2I_3I_4}sin\phi \tag{4.8}$$

where ϵ_0 is the electric field amplitude, Δk is the phase mismatch , $sin\phi = 1$ for perfect phase match, n is the refractive index and n_2 is the nonlinear-index coefficient, which is proportional to the real part of third-order susceptibility. Under the low depletion assumption and perfect phase matching, (4.8) calculates the output intensity of I_4 at distance l and the result scales with the input signal $I_1(0), I_2(0), I_3(0)$:

$$I_4(l) = \frac{4n_2^2\omega_4^2}{c^4\epsilon_0^2n^2}\frac{(1-\exp(-\frac{\alpha l}{2}))^2}{\alpha^2}I_1(0)I_2(0)I_3(0) \tag{4.9}$$

The natural exponentiation primitive can be realized with the Raman amplification process. When the signal is significantly smaller than the pump source and the nonlinear absorption is negligible, the output signal is solved as [20]:

$$I_s(l) = I_s(0)\exp(-\alpha l)\exp(g_RL_{eff}I_R(0)) \tag{4.10}$$

where l is the length of the amplifier and $L_{eff} = (1-\exp(-\alpha l))/\alpha$ is the effective length.

Exploiting the nonlinear optical properties native to silicon, we show an approach to create a logarithmic analog co-processor in silicon photonics. By engineering the relative strength of Raman amplification and nonlinear absorption, the sublinear relationship between signal input and output is tuned to emulate a logarithmic function. The logarithmic computing primitive, together with a scaling primitive and a natural exponentiation primitive, can be used sequentially to realize the extremely nontrivial analog optical exponentiation operation.

REFERENCES

[1] B. Murmann. ADC Performance Survey 1997-2018.

[2] R H Walden. Analog-to-digital converter survey and analysis. *IEEE Journal on Selected Areas in Communications*, 17(4):539–550, 1999.

[3] Ata Mahjoubfar, Dmitry V Churkin, Stéphane Barland, Neil Broderick, Sergei K Turitsyn, and Bahram Jalali. Time stretch and its applications. *Nature Photonics*, 11:341, jun 2017.

[4] K Goda and B Jalali. Dispersive Fourier transformation for fast continuous single-shot measurements. *Nature Photonics*, 7:102, jan 2013.

[5] Ali M Fard, Shalabh Gupta, and Bahram Jalali. Photonic time-stretch digitizer and its extension to real-time spectroscopy and imaging. *Laser & Photonics Reviews*, 7(2):207–263, jan 2013.

[6] K Goda, K K Tsia, and B Jalali. Serial time-encoded amplified imaging for real-time observation of fast dynamic phenomena. *Nature*, 458:1145, apr 2009.

[7] Ata Mahjoubfar, Keisuke Goda, Gary Betts, and Bahram Jalali. Optically amplified detection for biomedical sensing and imaging. *Journal of the Optical Society of America A*, 30(10):2124–2132, 2013.

[8] Brent Schwarz. Mapping the world in 3D. *Nature Photonics*, 4:429, jul 2010.

[9] Ming-Jie Sun, Matthew P Edgar, Graham M Gibson, Baoqing Sun, Neal Radwell, Robert Lamb, and Miles J Padgett. Single-pixel three-dimensional imaging with time-based depth resolution. *Nature Communications*, 7:12010, jul 2016.

[10] Christopher V. Poulton, Ami Yaacobi, David B. Cole, Matthew J. Byrd, Manan Raval, Diedrik Vermeulen, and Michael R. Watts. Coherent solid-state lidar with silicon photonic optical phased arrays. *Opt. Lett.*, 42(20):4091–4094, Oct 2017.

[11] J C Hulme, J K Doylend, M J R Heck, J D Peters, M L Davenport, J T Bovington, L A Coldren, and J E Bowers. Fully integrated hybrid silicon two dimensional beam scanner. *Optics Express*, 23(5):5861–5874, 2015.

[12] Steven A Miller, Christopher T Phare, You-Chia Chang, Xingchen Ji, Oscar A Jimenez Gordillo, Aseema Mohanty, Samantha P Roberts, Min Chul Shin, Brian Stern, Moshe Zadka, and Michal Lipson. 512-Element Actively Steered Silicon Phased Array for Low-Power LIDAR. In *Conference on Lasers and Electro-Optics*, OSA Technical Digest (online), page JTh5C.2, San Jose, California, 2018. Optical Society of America.

[13] G J Tearney, M Shishkov, and B E Bouma. Spectrally encoded miniature endoscopy. *Optics Letters*, 27(6):412–414, 2002.

[14] D R Solli, G Herink, B Jalali, and C Ropers. Fluctuations and correlations in modulation instability. *Nature Photonics*, 6:463, jun 2012.

[15] D R Solli, C Ropers, P Koonath, and B Jalali. Optical rogue waves. *Nature*, 450:1054, dec 2007.

[16] G Herink, B Jalali, C Ropers, and D R Solli. Resolving the build-up of femtosecond mode-locking with single-shot spectroscopy at 90MHz frame rate. *Nature Photonics*, 10:321, mar 2016.

[17] G Herink, F Kurtz, B Jalali, D R Solli, and C Ropers. Real-time spectral interferometry probes the internal dynamics of femtosecond soliton molecules. *Science*, 356(6333):50 LP – 54, apr 2017.

[18] E Roussel, C Evain, M Le Parquier, C Szwaj, S Bielawski, L Manceron, J.-B. Brubach, M.-A. Tordeux, J.-P. Ricaud, L Cassinari, M Labat, M.-E Couprie, and P Roy. Observing microscopic structures of a relativistic object using a time-stretch strategy. *Scientific Reports*, 5:10330, may 2015.

[19] C Evain, E Roussel, M Le Parquier, C Szwaj, M.-A. Tordeux, J.-B. Brubach, L Manceron, P Roy, and S Bielawski. Direct Observation of Spatiotemporal Dynamics of Short Electron Bunches in Storage Rings. *Physical Review Letters*, 118(5):54801, feb 2017.

[20] Claire Lifan Chen, Ata Mahjoubfar, Li-Chia Tai, Ian K Blaby, Allen Huang, Kayvan Reza Niazi, and Bahram Jalali. Deep Learning in Label-free Cell Classification. *Scientific Reports*, 6:21471, mar 2016.

[21] K Nakagawa, A Iwasaki, Y Oishi, R Horisaki, A Tsukamoto, A Nakamura, K Hirosawa, H Liao, T Ushida, K Goda, F Kannari, and I Sakuma. Sequentially timed all-optical mapping photography (STAMP). *Nature Photonics*, 8:695, aug 2014.

[22] Ata Mahjoubfar, Keisuke Goda, Ali Ayazi, Ali Fard, Sang Hyup Kim, and Bahram Jalali. High-speed nanometer-resolved imaging vibrometer and velocimeter. *Applied Physics Letters*, 98(10):101107, mar 2011.

[23] Jiang-Lai Wu, Yi-Qing Xu, Jing-Jiang Xu, Xiao-Ming Wei, Antony C S Chan, Anson H L Tang, Andy K S Lau, Bob M F Chung, Ho Cheung Shum, Edmund Y Lam, Kenneth K Y Wong, and Kevin K Tsia. Ultrafast laser-scanning time-stretch imaging at visible wavelengths. *Light: Science &Amp; Applications*, 6:e16196, jan 2017.

[24] Takakazu Suzuki Kannari, Ryohei Hida, Yuki Yamaguchi, Keiichi Nakagawa, Toshiharu Saiki, and Fumihiko. Single-shot 25-frame burst imaging of ultrafast phase transition of Ge 2 Sb 2 Te 5 with a sub-picosecond resolution. *Applied Physics Express*, 10(9):92502, 2017.

[25] Jens Buus, Markus-Christian Amann, and Daniel J. Blumenthal. Tunable laser diodes and related optical sources. New York: Wiley-Interscience, 2005.

[26] Claire Lifan Chen, Ata Mahjoubfar, and Bahram Jalali. Optical Data Compression in Time Stretch Imaging. *PLOS ONE*, 10(4):e0125106, apr 2015.

[27] Eric D Diebold, Nick K Hon, Zhongwei Tan, Jason Chou, Todd Sienicki, Chao Wang, and Bahram Jalali. Giant tunable optical dispersion using chromo-modal excitation of a multimode waveguide. *Optics Express*, 19(24):23809–23817, 2011.

[28] S Yegnanarayanan, P D Trinh, and B Jalali. Recirculating photonic filter: a wavelength-selective time delay for phased-array antennas and wavelength code-division multiple access. *Optics Letters*, 21(10):740–742, 1996.

[29] B Jalali and A Mahjoubfar. Tailoring Wideband Signals With a Photonic Hardware Accelerator. *Proceedings of the IEEE*, 103(7):1071–1086, 2015.

[30] Daniel R. Solli and Bahram Jalali. Analog optical computing. *Nature Photonics*, 9:704 EP –, 10 2015.

[31] R Huber, M Wojtkowski, and J G Fujimoto. Fourier Domain Mode Locking (FDML): A new laser operating regime and applications for optical coherence tomography. *Optics Express*, 14(8):3225–3237, 2006.

[32] Sebastian Karpf and Bahram Jalali. Frequency Doubled High Speed Fluorescence Lifetime Imaging. In *Conference on Lasers and Electro-Optics*, OSA Technical Digest (online), page STh3J.3, San Jose, California, 2018. Optical Society of America.

[33] K Takada, M Abe, T Shibata, and K Okamoto. 10-GHz-spaced 1010-channel tandem AWG filter consisting of one primary and ten secondary AWGs. *IEEE Photonics Technology Letters*, 13(6):577–578, 2001.

[34] Benjamin R Biedermann, Wolfgang Wieser, Christoph M Eigenwillig, and Robert Huber. Recent developments in Fourier Domain Mode Locked lasers for optical coherence tomography: Imaging at 1310 nm vs. 1550 nm wavelength. *Journal of Biophotonics*, 2(6?7):357–363, jul 2009.

[35] Sebastian Karpf, Matthias Eibl, Wolfgang Wieser, Thomas Klein, and Robert Huber. A Time-Encoded Technique for fibre-based hyperspectral broadband stimulated Raman microscopy. *Nature Communications*, 6:6784, apr 2015.

[36] Yunshan Jiang, Saili Zhao, and Bahram Jalali. Invited Article: Optical dynamic range compression. *APL Photonics*, 3(11):110806, nov 2018.

[37] Barry Lienert, John Porter, Norman Ahlquist, David Harris, and Shiv Sharma. A 50-MHz Logarithmic Amplifier for Use in Lidar Measurements. *Journal of Atmospheric and Oceanic Technology*, 19(5):654–657, may 2002.

[38] Alberto Tosi, Alberto Dalla Mora, Franco Zappa, Angelo Gulinatti, Davide Contini, Antonio Pifferi, Lorenzo Spinelli, Alessandro Torricelli, and Rinaldo Cubeddu. Fast-gated single-photon counting technique widens dynamic range and speeds up acquisition time in time-resolved measurements. *Optics Express*, 19(11):10735–10746, 2011.

[39] J. Chou, Y. Han, and B. Jalali. Time-wavelength spectroscopy for chemical sensing. *IEEE Photonics Technology Letters*, 16(4):1140–1142, April 2004.

[40] Eric D Diebold, Brandon W Buckley, Daniel R Gossett, and Bahram Jalali. Digitally synthesized beat frequency multiplexing for sub-millisecond fluorescence microscopy. *Nature Photonics*, 7:806, sep 2013.

[41] C Vinegoni, C Leon Swisher, P Fumene Feruglio, R J Giedt, D L Rousso, S Stapleton, and R Weissleder. Real-time high dynamic range laser scanning microscopy. *Nature Communications*, 7:11077, apr 2016.

[42] H C Gerritsen, M A H Asselbergs, A V Agronskaia, and W G J H M Van Sark. Fluorescence lifetime imaging in scanning microscopes: acquisition speed, photon economy and lifetime resolution. *Journal of Microscopy*, 206(3):218–224, jun 2002.

[43] Matthias Eibl, Sebastian Karpf, Daniel Weng, Hubertus Hakert, Tom Pfeiffer, Jan Philip Kolb, and Robert Huber. Single pulse two photon fluorescence lifetime imaging (SP-FLIM) with MHz pixel rate. *Biomedical Optics Express*, 8(7):3132–3142, 2017.

[44] Qinggong Tang, Yi Liu, Vassiliy Tsytsarev, Jonathan Lin, Bohan Wang, Udayakumar Kanniyappan, Zhifang Li, and Yu Chen. High-dynamic-range fluorescence laminar optical tomography (HDR-FLOT). *Biomedical Optics Express*, 8(4):2124–2137, 2017.

[45] Johannes Tiedau, Evan Meyer-Scott, Thomas Nitsche, Sonja Barkhofen, Christine Silberhorn, and Tim J Bartley. Measuring single photons to bright light with a logarithmic optical detector. In *Conference on Lasers and Electro-Optics*, OSA Terchnical Digest (online), page FW3F.6, San Jose, California, 2018. Optical Society of America.

[46] Yichen Shen, Nicholas C Harris, Scott Skirlo, Mihika Prabhu, Tom Baehr-Jones, Michael Hochberg, Xin Sun, Shijie Zhao, Hugo Larochelle, Dirk Englund, and Marin Soljačić. Deep learning with coherent nanophotonic circuits. *Nat Photon*, 11(7):441–446, jul 2017.

[47] Masahiro Nada, Takuya Hoshi, Hiroshi Yamazaki, Toshikazu Hashimoto, and Hideaki Matsuzaki. Linearity improvement of high-speed avalanche photodiodes using thin depleted absorber operating with higher order modulation format. *Optics Express*, 23(21):27715–27723, 2015.

[48] F Coppinger, S Yegnanarayanan, P D Trinh, and B Jalali. All-optical incoherent negative taps for photonic signal processing. *Electronics Letters*, 33(11):973–975, 1997.

[49] F Coppinger, A S Bhushan, and B Jalali. Time magnification of electrical signals using chirped optical pulses. *Electronics Letters*, 34(4):399–400, 1998.

[50] L Naval, B Jalali, L Gomelsky, and J M Liu. Optimization of Si/sub 1-x/Ge/sub x//Si waveguide photodetectors operating at /spl lambda/=1.3 /spl mu/m. *Journal of Lightwave Technology*, 14(5):787–797, 1996.

[51] Pao-Lo Liu, K J Williams, M Y Frankel, and R D Esman. Saturation characteristics of fast photodetectors. *IEEE Transactions on Microwave Theory and Techniques*, 47(7):1297–1303, 1999.

[52] D Dimitropoulos, S Fathpour, and B Jalali. Limitations of active carrier removal in silicon Raman amplifiers and lasers. *Applied Physics Letters*, 87(26):261108, dec 2005.

[53] B Jalali, D R Solli, K Goda, K Tsia, and C Ropers. Real-time measurements, rare events and photon economics. *The European Physical Journal Special Topics*, 185(1):145–157, 2010.

[54] J Chan, A Mahjoubfar, M Asghari, and B Jalali. Reconstruction in time-bandwidth compression systems. *Applied Physics Letters*, 105(22):221105, dec 2014.

[55] R M Gray and D L Neuhoff. Quantization. *IEEE Trans. Inf. Theor.*, 44(6):2325–2383, sep 2006.

[56] Bernard Smith. Instantaneous Companding of Quantized Signals. *Bell System Technical Journal*, 36(3):653–709, dec 1957.

[57] Peter T S DeVore Jalali, Daniel R Solli, David Borlaug, Claus Ropers, and Bahram. Rogue events and noise shaping in nonlinear silicon photonics. *Journal of Optics*, 15(6):64001, 2013.

[58] D Borlaug, S Fathpour, and B Jalali. Extreme Value Statistics in Silicon Photonics. *IEEE Photonics Journal*, 1(1):33–39, 2009.

[59] Yunshan Jiang, Peter T S DeVore, and Bahram Jalali. Analog optical computing primitives in silicon photonics. *Optics Letters*, 41(6):1273–1276, 2016.

[60] Yunshan Jiang, Peter T S DeVore, Ata Mahjoubfar, and Bahram Jalali. Analog Logarithmic Computing Primitives with Silicon Photonics. In *Conference on Lasers and Electro-Optics*, OSA Technical Digest (online), page JW2A.114, San Jose, California, 2016. Optical Society of America.

[61] Y Jiang, P T S DeVore, A Mahjoubfar, and B Jalali. Signal De-convolution with analog logarithmic computing primitives in silicon photonics. In *2016 IEEE Photonics Society Summer Topical Meeting Series (SUM)*, pages 70–71, 2016.

[62] M Sugawara, H Ebe, N Hatori, M Ishida, Y Arakawa, T Akiyama, K Otsubo, and Y Nakata. Theory of optical signal amplification and processing by quantum-dot semiconductor optical amplifiers. *Phys. Rev. B*, 69(23):235332, jun 2004.

[63] Jiaming Liu. Photonics devices. Cambridge University Press, 2005.

[64] Ozdal Boyraz and Bahram Jalali. Demonstration of a silicon Raman laser. *Optics Express*, 12(21):5269–5273, 2004.

[65] C. R. S. Fludger, V. Handerek, and R. J. Mears. Pump to signal rin transfer in raman fiber amplifiers. *Journal of Lightwave Technology*, 19(8):1140–1148, Aug 2001.

[66] B Jalali and S Fathpour. Silicon Photonics. *Journal of Lightwave Technology*, 24(12):4600–4615, 2006.

[67] R Claps, V Raghunathan, D Dimitropoulos, and B Jalali. Influence of nonlinear absorption on Raman amplification in Silicon waveguides. *Optics Express*, 12(12):2774–2780, 2004.

[68] X Sang, D Dimitropoulos, B Jalali, and O Boyraz. Influence of Pump-to-Signal RIN Transfer on Noise Figure in Silicon Raman Amplifiers. *IEEE Photonics Technology Letters*, 20(24):2021–2023, 2008.

[69] Dimitrios Dimitropoulos, Daniel R Solli, Ricardo Claps, Ozdal Boyraz, and Bahram Jalali. Noise Figure of Silicon Raman Amplifiers. *J. Light. Technol.*, 26(7):847–852, 2008.

[70] Amy C Turner-Foster, Mark A Foster, Jacob S Levy, Carl B Poitras, Reza Salem, Alexander L Gaeta, and Michal Lipson. Ultrashort free-carrier lifetime in low-loss silicon nanowaveguides. *Optics Express*, 18(4):3582–3591, 2010.

[71] Bahram Jalali and S. J. P Pearton. InP HBTs: growth, processing, and applications. Artech House Publishers, 1995.

[72] Jichi Ma, Jeff Chiles, Yagya D Sharma, Sanjay Krishna, and Sasan Fathpour. Two-photon photovoltaic effect in gallium arsenide. *Optics Letters*, 39(18):5297–5300, 2014.

[73] S Fathpour, K K Tsia, and B Jalali. Two-Photon Photovoltaic Effect in Silicon. *IEEE Journal of Quantum Electronics*, 43(12):1211–1217, 2007.

[74] Kevin K Tsia, Sasan Fathpour, and Bahram Jalali. Energy harvesting in silicon wavelength converters. *Optics Express*, 14(25):12327–12333, 2006.

[75] Sasan Fathpour and Bahram Jalali. Energy harvesting in silicon optical modulators. *Optics Express*, 14(22):10795–10799, 2006.

[76] S Fathpour, K K Tsia, and B Jalali. Energy harvesting in silicon Raman amplifiers. *Applied Physics Letters*, 89(6):61109, aug 2006.

[77] Varun Raghunathan, David Borlaug, Robert R. Rice, and Bahram Jalali. Demonstration of a mid-infrared silicon raman amplifier. *Opt. Express*, 15(22):14355–14362, Oct 2007.

[78] Lee W Tutt and Thomas F Boggess. A review of optical limiting mechanisms and devices using organics, fullerenes, semiconductors and other materials. *Progress in Quantum Electronics*, 17(4):299–338, 1993.

[79] Yuzhe Xiao, Haoliang Qian, and Zhaowei Liu. Nonlinear metasurface based on giant optical kerr response of gold quantum wells. *ACS Photonics*, 5(5):1654–1659, 2018.

[80] Haoliang Qian, Yuzhe Xiao, and Zhaowei Liu. Giant Kerr response of ultrathin gold films from quantum size effect. *Nature Communications*, 7:13153, oct 2016.

[81] H John Caulfield and Shlomi Dolev. Why future supercomputing requires optics. *Nature Photonics*, 4:261, may 2010.

[82] Anthony Tai, Thomas Cheng, and F T S Yu. Optical logarithmic filtering using inherent film nonlinearity. *Applied Optics*, 16(9):2559–2564, 1977.

[83] Toyohiko Yatagai, Kazuhiko Choji, and Hiroyoshi Saito. Pattern classification using optical Mellin transform and circular photodiode array. *Optics Communications*, 38(3):162–165, 1981.

[84] Samudra Roy, Shyamal K Bhadra, and Govind P Agrawal. Raman amplification of optical pulses in silicon waveguides: effects of finite gain bandwidth, pulse width, and chirp. *Journal of the Optical Society of America B*, 26(1):17–25, 2009.

[85] X Sang, En-kuang DTian, B Jalali, and Boyraz. Applications of two-photon absorption in silicon. *JOURNAL OF OPTOELECTRONICS AND ADVANCED MATERIALS*, 11(24):2021–2023, 2009.

[86] Hirohito Yamada Arakawa, Masayuki Shirane, Tao Chu, Hiroyuki Yokoyama, Satomi Ishida, and Yasuhiko. Nonlinear-Optic Silicon-Nanowire Waveguides. *Japanese Journal of Applied Physics*, 44(9R):6541, 2005.

[87] R. Claps, D. Dimitropoulos, V. Raghunathan, Y. Han, and B. Jalali. Observation of stimulated raman amplification in silicon waveguides. *Opt. Express*, 11(15):1731–1739, Jul 2003.

[88] R Soref and B Bennett. Electrooptical effects in silicon. *IEEE Journal of Quantum Electronics*, 23(1):123–129, 1987.

[89] Sungbong Park, Koji Yamada, Tai Tsuchizawa, Toshifumi Watanabe, Hiroyuki Shinojima, Hidetaka Nishi, Rai Kou, and Sei-ichi Itabashi. Influence of carrier lifetime on performance of silicon p-i-n variable optical attenuators fabricated on submicrometer rib waveguides. *Optics Express*, 18(11):11282–11291, 2010.

[90] Govind P Agrawal. Nonlinear Fiber Optics BT - Nonlinear Science at the Dawn of the 21st Century. pages 195–211, Berlin, Heidelberg, 2000. Springer Berlin Heidelberg.